Journal of proteome research

pubs.acs.org/jpr Article

DNAJA1 Dysregulates Metabolism Promoting an Antiapoptotic Phenotype in Pancreatic Ductal Adenocarcinoma

Heidi E. Roth,[▽] Fatema Bhinderwala,[▽] Rodrigo Franco, You Zhou, and Robert Powers*

Cite This: *J. Proteome Res.* 2021, 20, 3925−3939 Read Online

ACCESS | Metrics & More | Article Recommendations | Supporting Information

ABSTRACT: The cochaperone protein DNAJA1 (HSP40) is downregulated four-fold in pancreatic cancer cells. The impact of DNAJA1 expression on pancreatic ductal adenocarcinoma (PDAC) progression remains unclear. The metabolic impacts of increased DNAJA1 expression were evaluated using a combination of untargeted metabolomics, stable isotope-resolved metabolomics (SIRM), confocal microscopy, flow cytometry, and cell-based assays. Differential Warburg glycolysis, an increase in redox currency, and alterations in amino acid levels were observed in both overexpression cell lines. DNAJA1 overexpression also led to mitochondrial fusion, an increase in the expression of Bcl-2, a modest protection from redox-induced cell death, a loss of structural integrity due to the loss of actin fibers, and an increase in cell invasiveness in BxPC-3. These differences were more pronounced in BxPC-3, which contains a loss-of-function mutation in the tumor-suppressing gene SMAD4. These findings suggest a proto-oncogenic role of DNAJA1 in PDAC progression and suggest DNAJA1 may function synergistically with other proteins with altered activities in pancreatic cancer cell lines.

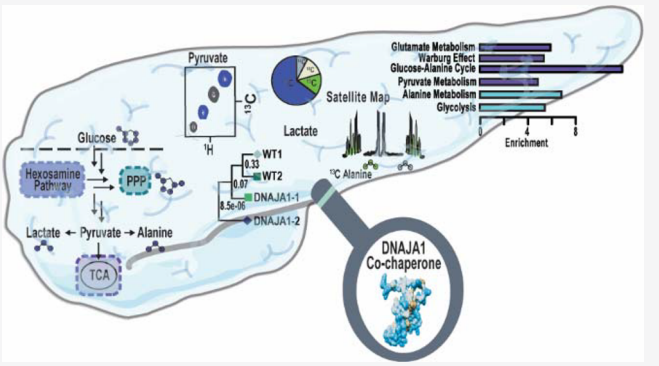

KEYWORDS: *pancreatic cancer, metabolomics, NMR, DNAJA1, glycolysis, cochaperones*

INTRODUCTION

Pancreatic ductal adenocarcinoma (PDAC) characteristically presents high lethality rates and an abysmal five-year survival prognosis.[1] Treatments for advanced stages of PDAC remain largely ineffective with no improved therapies seen in over three decades.[2] Beyond surgical intervention, there are limited drug regimens that are effective against PDAC, such as the nucleoside analogs gemcitabine and 5-fluorouracil.[3] Unfortunately, these chemotherapy treatments demonstrate a low 20% effectiveness due to acquired chemotherapeutic resistance in most PDAC patients.[3] Poor survival outcomes and treatment challenges are driving forces to identify new PDAC targets in order to develop alternative therapies and resolve existing challenges in PDAC management.[4] Metabolic dysregulation has been described as the basis of cancer pathology[5−7] with nearly all forms of PDAC characterized by aberrant aerobic glycolysis and glutaminolysis.[8] Analyzing the regulatory roles of these pathways has presented promising nonchemotherapeutic PDAC treatment potential.[8]

Metabolomics-driven cancer research focuses on identifying specific diagnostic and therapeutic targets across phenotypes.[9] Through global untargeted metabolomics and stable isotope-resolved metabolomics (SIRM) experiments,[10] metabolic fluxes can be used to define aberrant pathways prominent in PDAC and the consequences of this dysregulation.[9] Metabolomics is rapidly becoming an indispensable tool of cell biology research and for the drug discovery process. Metabolomics analyses of PDAC may benefit *in vivo* drug efficacy, mechanisms of drug action, drug metabolism, toxicology, and the identification and evaluation of druggable targets.[11] Metabolic dysregulation in PDAC may also result in multiple-drug resistance while contributing to other conditions unique to the carcinogenic state.[11]

The heat shock protein 40 (HSP40) family is most often cited as cochaperones of HSP70.[12] Chaperone activity is critical to a range of cellular functions with HSP40s increasingly recognized as valuable to cancer research due to their potential as therapeutic targets. Members of the HSP40 family of proteins often chaperone other proteins commonly classified as tumor-suppressing or oncogenic.[13] Proteomic profiling of cancerous and normal pancreatic tissues has identified a greater than four-fold downregulation in the expression of the HSP40 member DNAJA1.[14] DNAJA1 has been shown to impact p53 localization and antiapoptosis activity, increase tumorigenicity, and mediate macro-autoph-

Received: March 23, 2021
Published: July 15, 2021

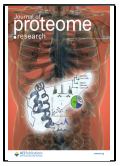

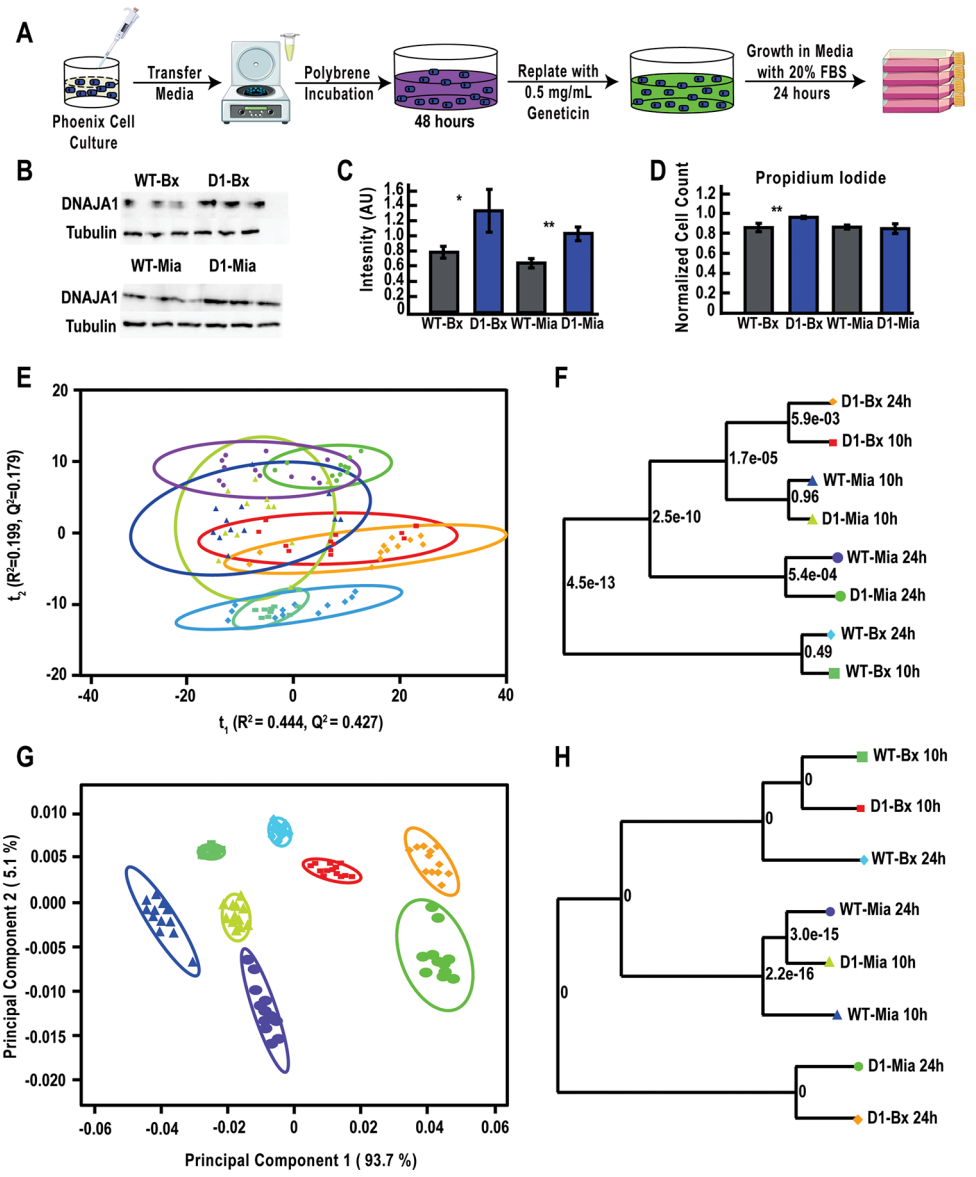

Figure 1. DNAJA1 overexpression imparts a unique metabolic profile in pancreatic cancer cells. (A) Schematic summarizing the generation of stable DNAJA1-overexpressing PDAC cells. Images in this figure are free medical images from Servier Medical Art (https:/smart.servier.com/) under the Creative Commons License Attribution 3.0 Unported (CC BY 3.0). (B) Western immunoblot analysis showing the successful overexpression of DNAJA1. (C) Bar graph quantifying DNAJA1 expression in WT and D1 cells from the Western immunoblots in (B). Data are plotted as an average of triplicate measurements (n = 3) with standard deviations represented as brackets. WT bars are colored gray, and D1 bars are colored blue. Univariate pairwise comparisons used Student's t test with p-values indicated as $^{*}p < 0.05$ and $^{**}p < 0.01$. (D) Bar graph quantifying cell viability in WT and D1 cells. (E) PCA score plot generated from 1D ^{1}H NMR spectra of cell lysates of WT and D1 cell lines of BxPC-3 and MIA PaCa-2 (R^2 of 0.643, Q^2 of 0.606). The ellipse around each cluster corresponds to the 95% confidence interval for a normal distribution of data. Each cluster contains 12 replicates, except for WT-Bx at 10 h where n = 9 and D1-Mia at 24 h where n = 11. (F) Metabolic tree diagram generated from the PCA score plot in (E). The p-value at each node is calculated from the Mahalanobis distance between each group. The coloring is identical between the PCA score plot and the tree diagram. (G) PCA score plot generated from peak intensities in the 2D ^{1}H−^{13}C NMR spectra for cell lysates of both WT and D1 cell lines (R^2 of 0.989, Q^2 of 0.988). (H) Metabolic tree diagram generated from the PCA score plot in (F). The color scheme is as follows: WT-Bx cells at 10 h (green squares) and at 24 h (blue diamonds) and D1-Bx cells at 10 h (red squares) and at 24 h (orange diamonds). Similarly, WT-Mia at 10 h (blue triangles) and at 24 h (purple circles) and D1-Mia at 10 h (chartreuse triangles) and at 24 h (green circles).

agy.[15−18] These cellular functions attributed to familial subclass A have piqued interest in the role that DNAJA1 plays in PDAC and its value as a therapeutic target.

Due to the downregulation of DNAJA1 in cancerous pancreatic tissues, increased DNAJA1 expression was induced in PDAC cells to investigate its impact on cellular functions.[14] We previously reported the high-resolution NMR structure of the DNAJA1 J-domain and noted that the overexpression of DNAJA1 in MIA PaCa-2 cells modulated a stress response.[17] Here, we report our further investigation into the cellular response from overexpression of DNAJA1 in PDAC cell lines, BxPC-3 and MIA PaCa-2, and its impact in pancreatic cancer metabolism. Through an NMR-based metabolomics approach, we have identified differential metabolism in DNAJA1-overexpressing (D1) pancreatic cancer cell lines. In these D1 cells, we observed significant dysregulation in fundamental

https://doi.org/10.1021/acs.jproteome.1c00233
J. Proteome Res. 2021, 20, 3925−3939

metabolic pathways, marginal loss of mitochondrial dispersion, and loss of lysosomal integrity, which collectively impacted cellular survival. DNAJA1 overexpression exhibits a distinct impact on tumor-specific metabolic processes like aerobic glycolysis and glutaminolysis, which is coupled with a response specific to the two phenotypically unique pancreatic cancer cells.[8,19,20]

MATERIALS AND METHODS

Cell Culture for Establishing Wild-Type (WT) DNAJA1-Overexpressing Cell Lines (D1)

BxPC-3 (WT-Bx) and MIA PaCa-2 (WT-Mia) were purchased from the American Type Culture Collection (ATCC) and cultured following ATCC guidelines. For DNAJA1 overexpression, Phoenix cells obtained from Dr. Pankaj Singh at the University of Nebraska Medical Center containing the DNAJA1 plasmid were grown following a standard ATCC protocol, and viral particles were isolated as previously described.[21] Wild-type cells were transfected as previously described.[22,23] Transfected BxPC-3 (D1-Bx) and MIA PaCa-2 (D1-Mia) cell lines were grown and maintained in 20% FBS. Briefly as shown in Figure 1A, Phoenix cells were incubated for 48 h before removing media containing the retroviral particles. Media were clarified of cellular debris, and viral particles were pelleted. The pellet was resuspended in PDAC growth media containing polybrene to increase retroviral transfection efficiency. PDAC cells and the viral particles were incubated for 48 h. PDAC cells were then washed of viral media and replated with the selective agent Geneticin. PDAC cells were washed of Geneticin after 24 h incubation and maintained in a growth medium containing 20% FBS.

Cell Culture Growth and Extraction of Polar Metabolites for NMR Metabolomics

Wild-type and transfected cell lines were seeded at 300,000 cells in six-well plates and grown to ∼80% confluency in replicates of 12. Cells were extracted 10 and 24 h after addition of media containing 99.8% ^{13}C-U-glucose at 25 mM. MIA PaCa-2 was cultured in DMEM, with 10% FBS, 4 mM L-glutamine, and 25 mM ^{13}C-$_6$glucose. BxPC-3 was cultured in RPMI, with 10% FBS, 2.05 mM L-glutamine, and 25 mM $^{13}C_6$-glucose. PDAC cell growth relies on glucose and noncanonical glutamine metabolism,[24] so these high glucose and glutamine concentrations were maintained from cell culturing through metabolome extraction. This prevents nutrient stress and erroneous metabolite alterations when switching from a standard growth medium to SILAC media for SIRM. Media were aspirated and saved for analysis, and cells were lysed using 1 mL of an 80% methanol/water mixture at −80 °C followed by incubation for 15 min at −80 °C. To ensure complete detachment, plates were scraped then transferred to a 2 mL microtube. The cell lysate was centrifuged at 16,200*g* for 5 min, and the supernatant was collected and transferred to a new microtube. The cell pellet was rinsed with 500 μL of the 80% methanol/water mixture, centrifuged, decanted, and repeated with 500 μL of ice-cold water. Five hundred microliters of media was allocated for analysis after being cleared of cellular debris by centrifugation at 500*g* for 5 min. Lysate and medium supernatants were dried by vacuum evaporation (SpeedVac Plus, Savant, Thermo Scientific, Waltham, MA) followed by freeze-drying (Labconco, Kansas City, MO).

NMR Sample Preparation

Cell lysates were reconstituted in 160 μL of 50 mM phosphate buffer, and medium extracts were reconstituted in 550 μL of 50 mM phosphate buffer prepared at pH 7.2 uncorrected with 500 μM 3-(tetramethylsilane) propionic acid-2,2,3,3-D_4 (TMSP-D_4) added as a chemical shift reference made in 99.8% D_2O. Lysate and medium samples were resuspended by vortexing and centrifuged at 16,200*g* for 5 min to pellet any insoluble particulates and tracer impurities. Lysate samples were transferred into 3 mm tubes to obtain a higher concentration of metabolite extracts and improve the overall sensitivity of low-concentration metabolites during NMR experiments. Media samples were transferred into 5 mm tubes as these spent media typically provide excellent NMR spectra in a reasonable time using 5 mm tubes.

NMR Data Collection

All data were collected on a Bruker Avance III-HD 700 MHz spectrometer equipped with a quadruple resonance QCI-P cryoprobe (^{1}H, ^{13}C, ^{15}N, and ^{31}P with ^{2}H lock and decoupling) and a SampleJet automated sample changer. For media samples, the 1D ^{1}H NMR spectra were collected at 298 K with 32K data points, 128 scans, 4 dummy scans, and a spectral width of 9090 Hz using an excitation sculpting pulse sequence.[25] Fifty percent nonuniformly sampled (NUS) deterministic burst augmented gap schedule[26] 2D ^{1}H−^{13}C HSQC NMR experiments were collected with 2K data points and a spectral width of 9090 Hz in the direct dimension and 128 data points with a spectral width of 29,059 Hz in the indirect dimension. For lysates, the 1D ^{1}H NMR spectra were collected at 298 K with 32K data points, 200 scans, 4 dummy scans, and a spectral width of 11,160 Hz using an excitation sculpting pulse sequence.[25] Fifty percent nonuniformly sampled (NUS) 2D ^{1}H−^{13}C HSQC NMR experiments were collected with 1K data points and a spectral width of 11,160 Hz in the direct dimension and 128 data points with a spectral width of 29,059 Hz in the indirect dimension.

NMR Data Processing and Analyses

Our MVAPACK software (http://bionmr.unl.edu/mvapack.php) was used to analyze the NMR metabolomics data.[27] A principal component analysis (PCA) model was generated from the 1D ^{1}H NMR dataset. The 1D ^{1}H NMR spectra were Fourier transformed, automatically phased, and binned using adaptive intelligent binning.[28] The dataset was normalized using constant integral normalization, the noise was removed as previously described, and the dataset was scaled using Pareto scaling.[29] The tree diagram was generated from the PCA score plot using our PCA/PLS-DA utilities as previously described.[30] Lysate spectra contained one outlier in D1-Mia at 24 h and three outliers in WT-Bx at 10 h. Media contained one WT-Mia outlier at 10 h. The orthogonal projections to latent structures discriminant analysis (OPLS-DA) score plot and back-scaled loadings were generated using the entire NMR spectra following alignment with the icoshift algorithm[31] and removal of solvent peaks (4.65−4.85 ppm for water) as deemed necessary. The 2D ^{1}H−^{13}C HSQC NMR spectra were processed using NMRPipe with sparse multidimensional iterative lineshape-enhanced (SMILE) reconstruction and then analyzed using NMRViewJ.[32−34] The Human Metabolome Database, the Platform for RIKEN Metabolomics, the Madison Metabolomics Consortium, and Chenomx NMR Suite 8.0 (http://www.chenomx.com/) were used for metabolite identification.[35−37] Metabolite changes presented are

https://doi.org/10.1021/acs.jproteome.1c00233
J. Proteome Res. 2021, 20, 3925−3939

evaluated using Student's t test, and multiple hypotheses were corrected using the Benjamini−Hochberg method. Other statistical analysis details are listed under each figure as needed. Metabolites were assigned using 0.08 and 0.25 ppm chemical shift errors for ^{1}H and ^{13}C resonances, respectively. Accordingly, metabolites were identified to MSI level 2.[38] Peak intensities were sum normalized using the total intensity of the spectrum. All normalized peaks were then used to generate the PCA models for the 2D $^{1}H-^{13}C$ NMR data. PCA models and heat maps were generated using MetaboAnalyst 4.0.[39]

Cell Viability Assay

Cell viability was quantified using the CyQUANT XTT cell viability assay from Thermo Fisher Scientific following a standard protocol. Cells were plated in triplicate in 96-well plates at 15,000 cells per well and grown as discussed above. Cells were subjected to H_2O_2 to assess ROS response with concentrations of 0, 100, 250, 350, 450, and 500 μM H_2O_2. Cells were incubated for 4 h and read on a BioTek Synergy HTX multimode microplate reader at wavelengths of 450 and 660 nm.

Validation of DNAJA1 Overexpression by Protein Extraction, Electrophoresis, and Western Immunoblotting

Protein extraction, SDS-PAGE electrophoresis, and Western immunoblotting were performed as previously described.[40] Membranes were blocked and probed with primary antibodies according to manufacturer recommendations. Antibodies used include DNAJA1 (HDJ2) [KA2A5.6 (Invitrogen)], BCL-2, β-actin, and β-tubulin [BT7R (Invitrogen)]. An equal protein loading was verified with β-tubulin. Relative densitometric analysis of blots was completed using ImageJ.[41] Images of the full membranes are available in the Supporting Information as Figures S6 to S9.

Confocal Microscopy

Cells were cultured in 35 mm Petri dishes with 20 mm glass-bottom microwells to ∼80% confluency. Cultures were then incubated with 5 μM MitoTracker Red and 5 μM LysoTracker Deep Red in serum-free, nonsupplemented DMEM for 30 min at 37 °C and 5% CO_2. After replacing with a fresh culture medium, DMEM with 10% FBS, the cells were placed in a live-cell imaging humidified chamber (controlled at 37 °C and 5% CO_2), and 4−5 random images were collected (or a time course of the region of cells) using sequential mode of the Nikon NIS-Element program with a Nikon A1r-Ti2 advanced confocal system. For comparing morphology and structures between wild-type and D1-overexpressing cells, samples were fixed in 4% paraformaldehyde in PBS at room temperature for 30 min. Since the D1-overexpressing cells have poor adherence and easily detached compared to wild-type, 1% ethanol was added to the fixative. Cultures were then stained with Alexa Fluor 488−phalloidin and DAPI in PBS at room temperature for 30 min. Images were captured using a microscope with sequential, dual excitation (405 and 488 nm) and dual emission (420 and 520 nm) using the confocal system. All images for comparisons between groups were collected under the same confocal settings and under the same labeling conditions.

Flow Cytometry

Cells were grown as described above and stained using ThiolTracker Violet [T10095 (Invitrogen)] at 10 μM and propidium iodide at 1.5 μM [P1304MP (Invitrogen)]. A 561 nm laser was used for excitation, and a 620/20 band pass filter was used for detection of PI fluorescence. A 407 nm laser was used for excitation, and a 545/30 band pass filter was used for detection of ThiolTracker Violet fluorescence. Ten thousand events per sample were recorded with median fluorescence of ThiolTracker Violet only recorded for live cells. Data was collected on a Cytek DxP10 operated by FlowJo CE and analyzed in FlowJo 10.6 by Becton Dickinson.

Invasion Assay

In order to assess the role of DNAJA1 overexpression in cell metastasis, CytoSelect 24-well cell invasion assay [CBA-111 (Cell Biolabs, Inc.)] was used to quantify DNAJA1's role in invasion using the basement membrane in a fluorometric format. Cells were seeded at 215,000 per upper chamber and incubated for 24 h at 37 °C and 5% CO_2 before following a standard digestion protocol. Briefly as depicted in Figure 6D, PDAC cells were placed in an isolated chamber containing serum-free media with a basement membrane on the bottom of the chamber. This chamber was surrounded by standard growth media and incubated for 24 h. Cells that were able to migrate through the basement membrane and had adhered to the chamber surface were dissociated and lysed for quantification. Fluorescence was measured using a Synergy HTX multimode microplate reader at 485/528 nm.

RESULTS AND DISCUSSION

DNAJA1 Overexpression in Pancreatic Cancer Cell Lines Induces Time-Dependent Metabolic Changes

Wild-type (WT) cells of human pancreatic cancer lines BxPC-3 (WT-Bx) and MIA PaCa-2 (WT-Mia) were retrovirally transduced using purified viruses produced from Phoenix cells coding for DNAJA1 to generate the overexpression BxPC-3 (D1-Bx) and MIA PaCa-2 (D1-Mia) cell lines (Figure 1A). Overexpression of DNAJA1 was confirmed by Western immunoblot analysis (Figure 1B) and quantified, showing a significant increase in expression compared to the wild type (Figure 1C). Live versus dead cell populations were determined by flow cytometry using propidium iodide staining (Figure 1D).

WT and D1 cells were cultured using $^{13}C_6$-glucose as an isotope tracer to study the metabolic changes induced by DNAJA1. Polar metabolites were extracted from the cell lysates, and 1D ^{1}H NMR and 2D $^{1}H-^{13}C$ HSQC spectra were collected for each biological replicate (n = 12). The 1D ^{1}H NMR metabolomics datasets were then analyzed using multivariate statistical methods to demonstrate global metabolic differences between WT and D1 cell lines. An unsupervised PCA model (Figure 1E, R^2 of 0.643 and Q^2 of 0.606) illustrates the four groups (WT-Bx, D1-Bx, WT-Mia, and D1-Mia), and two time points (10 and 24 h) are mostly separated into distinct clusters signifying metabolic changes arising from DNAJA1. Importantly, these metabolic differences are likely due to the cellular activity of DNAJA1 instead of a generic response to the process of overexpressing a protein. A number of prior studies have failed to identify any metabolic signature associated with the overexpression of a protein in a cell line.[42,43]

A tree diagram (Figure 1F) derived from the score plot (Figure 1E) indicates that the intracellular metabolomes of WT-Bx and D1-Bx are phenotypically distinct as evidenced by their leaves being the furthest apart in the dendrogram (p = 4.5 × 10^{-13}). The global intracellular metabolomes of WT-Mia and D1-Mia clustered based upon cell culture time as well as

https://doi.org/10.1021/acs.jproteome.1c00233
J. Proteome Res. 2021, 20, 3925−3939

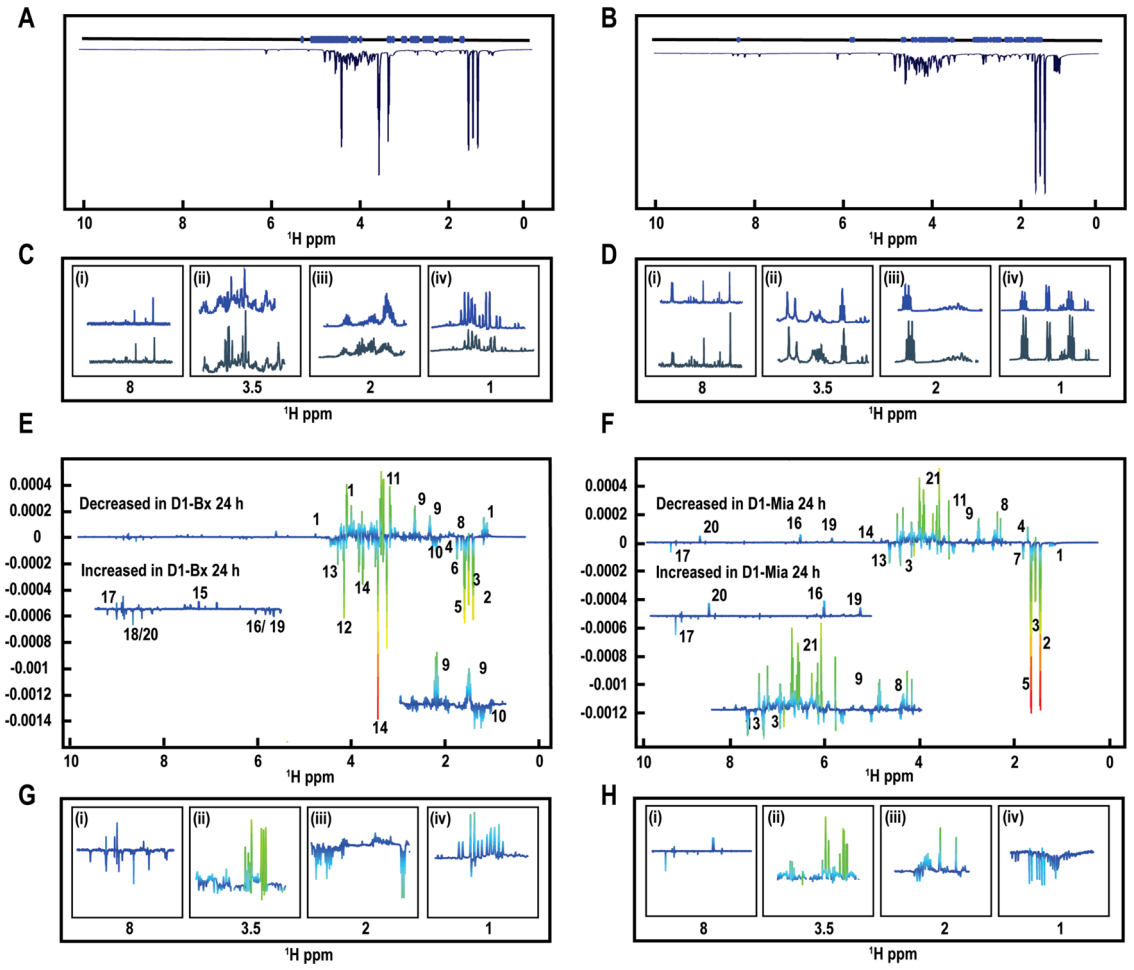

Figure 2. Global metabolic changes observed following DNAJA1 overexpression. Mean 1D ^{1}H NMR spectra of wild-type (A) BxPC-3 and (B) MIA PaCa-2 cells marked with blue points indicating the significantly altered ($p < 0.001$) NMR spectral bins in the corresponding 1D ^{1}H NMR spectrum for D1 cells. Expanded views of the mean 1D ^{1}H NMR spectrum with WT shown in gray (bottom) and D1 shown in blue (top) for (C) WT-Bx and D1-Bx and (D) WT-MIA and D1-Mia. The panels in (C) and (D) correspond to (i) branched-chain amino acids, (ii) glutamine and glutamate, (iii) glucose, and (iv) energy metabolites. Back-scaled loading plots comparing (E) WT-Bx to D1-Bx and (F) WT-Mia to D1-Mia at the 24 h time point. The back-scaled loading plots in (E) and (F) were generated from valid OPLS-DA models: an R^2 of 0.999, a Q^2 of 0.982, and a CV-ANOVA p-value of 1.2×10^{-13} and an R^2 of 0.997, a Q^2 of 0.989, and a CV-ANOVA p-value of 7.27×10^{-14}, respectively. Positive peaks identify spectral features increased in WT, and negative peaks are decreased in WT. Peaks observed in the back-scaled loading plots are numbered as follows: 1, branched-chain amino acids (leucine, isoleucine, and valine); 2, lactate; 3, alanine; 4, acetate; 5, 3-hydroxybutyrate; 6, aminobutyrate; 7, lysine; 8, arginine; 9, glutamine; 10, glutamate; 11, aspartate; 12, cystathionine; 13, proline; 14, glucose; 15, aromatic amino acids (tyrosine and phenylalanine); 16, $NADP^+$; 17, NADH; 18, AXP; 19, CXP; 20, UXP and UXP-glucose; 21, myo-inositol. (G,H) Expanded views of the back-scaled loading plots of (E) and (F). The panels in (G) and (H) correspond to (i) branched-chain amino acids, (ii) glutamine and glutamate, (iii) glucose, and (iv) energy metabolites.

DNAJA1 expression, indicating metabolome perturbations accumulated over time. However, the tree diagram indicates that the metabolome of WT-Bx cells did not change over time. The p-value based on the Mahalanobis distance between the WT-Bx 24 h and the WT-Bx 10 h groups was insignificant ($p = 0.49$). Conversely, a modest difference ($p = 5.9 \times 10^{-3}$) was observed between the D1-Bx 24 h and the D1-Bx 10 h groups, suggesting that the DNAJA1-induced metabolic difference between WT-Bx and D1-Bx accumulates over time. For the MIA PaCa-2 cell lines, the metabolic difference between WT-Mia and D1-Mia at 10 h was not significant (p-value of 0.96) but became significant (p-value of 5.4×10^{-4}) at 24 h. The group separation variation indicates that these metabolic differences are impacted by DNAJA1, cell genotype, and cell culture time.

A PCA score plot (Figure 1G) was generated from the 2D ^{1}H−^{13}C heteronuclear single quantum coherence (HSQC) spectral peak intensities (R^2 of 0.989, Q^2 of 0.988) using MetaboAnalyst 4.0.[39] The corresponding tree diagram (Figure 1H) was generated using the scores from the 2D ^{1}H−^{13}C HSQC PCA model (Figure 1G). The PCA score plots and tree diagram primarily highlight differences in glucose metabolism and central carbon metabolism. Statistically significant separation was observed between all groups and time points, where the p-values in the dendrogram were zero or near zero. The dendrogram highlights that cell type-driven metabolic variations between the BxPC-3 cells and the MIA Pa Ca-2 dominated over DNAJA1 overexpression at an early time point. The subsequent accumulation of DNAJA1-related metabolic changes overrode cell type metabolic variations at 24 h. At 10 h, D1-Bx and D1-Mia clustered with their wild-type

https://doi.org/10.1021/acs.jproteome.1c00233
J. Proteome Res. 2021, 20, 3925−3939

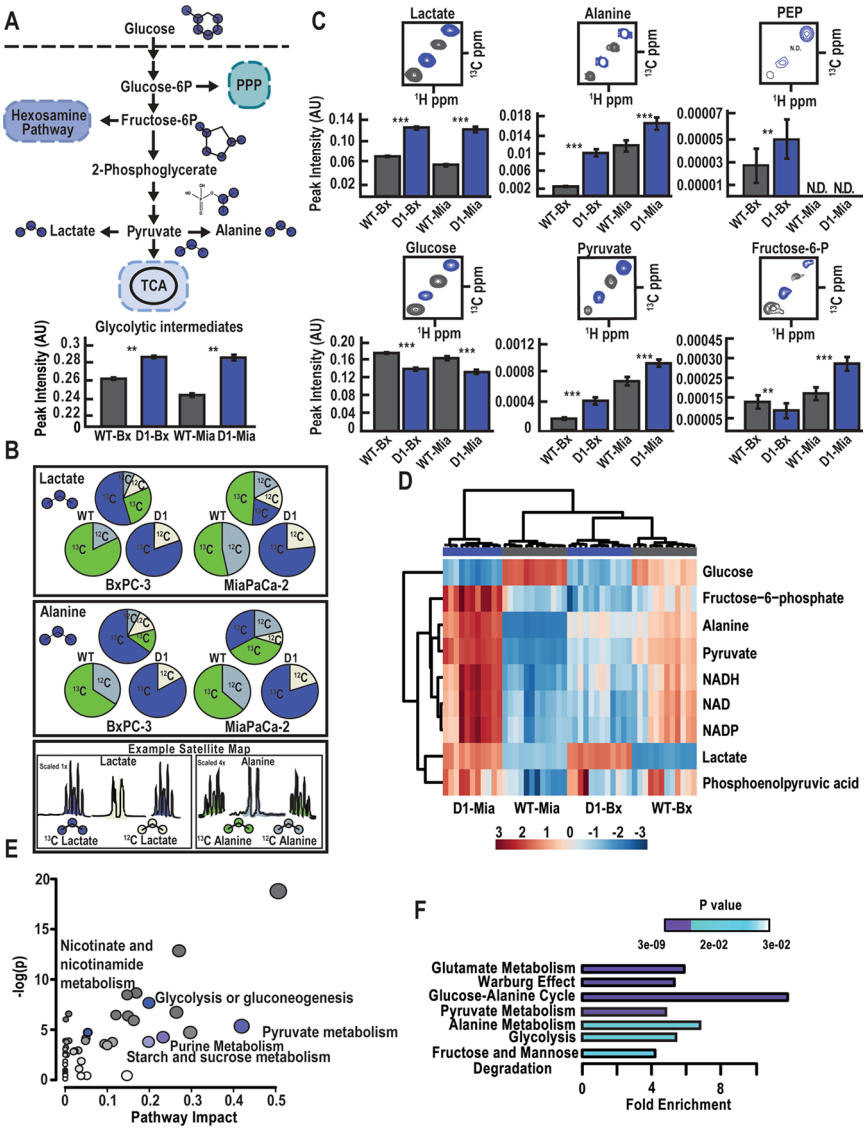

Figure 3. DNAJA1 alters aerobic glycolysis and encourages diverse glucose utilization. (A) (top) Schematic of the glycolytic pathway, which illustrates the major regulatory steps, the location of ^{13}C carbons in metabolites derived from $^{13}C_6$-glucose, and the metabolic products of aerobic glycolysis. The blue circles overlaid on the chemical structures identify the location of ^{13}C carbons. (bottom) Bar graph plotting the sum of NMR peak intensities for all glycolytic intermediates obtained from 2D $^{1}H-^{13}C$ HSQC spectra. WT bars are colored gray, and D1 bars are colored blue. A statistically significant increase in glycolysis resulted from DNAJA1 overexpression. (B) Pie charts summarizing the fractional ^{13}C enrichment of lactate (top panel) and alanine (middle panel) catabolized from $^{13}C_6$-glucose. The fractional ^{13}C enrichment was determined from the ^{13}C satellite peaks in 1D ^{1}H NMR spectra. Fractions of ^{12}C and ^{13}C metabolites are represented by each arc length. The pie charts corresponding to WT (bottom left pie chart) are colored green for ^{13}C and gray for ^{12}C, D1 (bottom right chart) are colored blue for ^{13}C and cream for ^{12}C, and WT+D1 (top middle pie chart) is a composite of the two bottom pie charts using the same color scheme as the individual WT and D1 pie charts. (bottom panel) Expanded views of representative 1D ^{1}H NMR spectra highlighting selected (left) lactate and (right) alanine $^{1}H-^{12}C$ and $^{1}H-^{13}C$ peaks. The ^{13}C satellites are scaled relative to the $^{1}H-^{12}C$ peaks. The ^{13}C satellites are colored blue for lactate and green for alanine. The $^{1}H-^{12}C$ peaks are colored cream for lactate and gray for alanine. The same color scheme is used to highlight the ^{12}C and ^{13}C atoms in the chemical structures below the NMR spectra. A variable enrichment in $^{13}C_6$-glucose-derived ^{13}C lactate and ^{13}C alanine resulted from DNAJA1 overexpression. (C) Expanded view of overlaid 2D $^{1}H-^{13}C$ HSQC spectra and the associated bar charts for WT and D1 cells. Bar charts highlight the significant metabolic shift in metabolites derived from $^{13}C_6$-glucose. Data are plotted as the average peak intensity from 2D $^{1}H-^{13}C$ HSQC spectra with standard deviations represented as brackets (n = 12). WT bars and HSQC peak contours are colored gray, and D1 bars and HSQC peak contours are colored blue. (D) Heat map and hierarchical clustering of glycolytic intermediates. The heat map plots normalized peak intensities from 2D $^{1}H-^{13}C$ HSQC spectra. Each row displays the relative metabolite abundance across the four groups, where red identifies a relative metabolite accumulation and blue indicates metabolite depletion. (E) Pathway impact plot based on metabolite occurrence from the analysis of the 2D $^{1}H-^{13}C$ HSQC spectra. (F) Pathway enrichment plot based on metabolite concentrations from the analysis of the 2D $^{1}H-^{13}C$ HSQC spectra. Pathway fold enrichment is colored according to the corresponding p-value using the indicated purple to teal scale. Pathways were selected to highlight the intracellular metabolic variations linked to glucose metabolism. See Figure S4 for the complete list of pathways enriched by DNAJA1 overexpression. The pathway impact and enrichment plots were generated using MetaboAnalyst 4.0 (https://www.metaboanalyst.ca/). Univariate pairwise comparisons used Student's t test followed by a Benjamini−Hochberg multiple-hypothesis correction. The corrected p-values are indicated as $^{*}p < 0.05$, $^{**}p < 0.01$, $^{***}p < 0.001$, and $^{\#}p < 0.0001$.

https://doi.org/10.1021/acs.jproteome.1c00233
J. Proteome Res. 2021, 20, 3925−3939

counterparts while still being significantly different. The impact due to DNAJA1 overexpression was minimal relative to the cell type differences at 10 h. This changed at the 24 h time point, where D1-Bx and D1-Mia clustered together on a separate and distinct branch. The D1-overexpressing cell lines were distinct from their respective wild type, as well as the profile at 10 h, i.e., the early time point. Glucose metabolism dominated the metabolic impact of DNAJA1 overexpression at 24 h.

A similar set of multivariate analyses were performed on the spent media from all cell cultures. The resulting PCA score plots and associated tree diagrams are available in the Supporting Information (Figure S1). The extracellular changes evident from the 1D ^{1}H NMR spectra (Figure S1A,B) and the 2D ^{1}H−^{13}C NMR spectra (Figure S1C,D) once again show time-dependent metabolomic variances, the impact of DNAJA1 overexpression, and the impact of phenotypic differences on the metabolome. A nearly identical group clustering pattern is observed when comparing the statistical models describing the extracellular and intracellular metabolomes. This supports a direct coupling between excreted metabolites and intracellular metabolome changes. Collectively, these data confirm the successful overexpression of DNAJA1 in BxPC-3 and MIA PaCa-2 and that the overexpression impacts both global metabolism and glucose utilization.

DNAJA1 Overexpression Imparts a Distinct Global Metabolic Profile to Pancreatic Cancer Cells

Altered metabolites due to DNAJA1 overexpression were identified by comparing spectral bins from WT and D1 1D ^{1}H NMR spectra.[28] Statistically significant ($p < 0.001$) bin changes are marked on the mean 1D ^{1}H spectra from WT-Bx and WT-Mia cell lysates (Figure 2A,B). Overlays of expanded regions of the 1D ^{1}H NMR spectra from WT and D1 are shown in Figure 2C,D. The expanded regions demonstrate variable peak intensities corresponding to changes in branched-chain amino acids, glutamine and glutamate, glucose, and energy metabolite concentrations.

Orthogonal projections to latent structures discriminant analysis (OPLS-DA) models were also generated from the 1D ^{1}H NMR spectra of the cell lysate and spent media. A supervised OPLS-DA model comparing WT and D1 metabolomes further aided in the identification of metabolite changes arising from group specific separation. The resulting OPLS-DA models from WT and D1 NMR datasets were of high statistical quality and significance (Figure S3). Loadings contributing to the group-dependent separation were extrapolated from the OPLS-DA models and visualized as back-scaled loadings or pseudo-1D ^{1}H NMR spectra (Figure 2E,F). The back-scaled loading plots from the pairwise comparisons of the cell lysates from WT and D1 (24 h) for BxPC-3 and MIA PaCa-2 are shown in Figure 2E,F. Expanded views of BxPC-3 and MIA PaCa-2 back-scaled loading plots highlight key intracellular changes (Figure 2G,H).

The comparison of WT-Bx and D1-Bx cell lysates identified a total of 25 key metabolite changes (Figure 2E,G). WT-Mia and D1-Mia cellular metabolomes presented a similar set of altered metabolites to WT- and D1-Bx, as well as a subset of metabolites unique to MIA PaCa-2 cells. These metabolites included significantly increased glycolytic intermediates including lactate, alanine, and glucose in D1 cells. Conversely, branched-chain amino acid levels were decreased in D1-Bx cells compared to an increase in D1-Mia cells. DNAJA1 induced cell type-specific changes to the cellular concentration of nucleotide bases, with a decrease in adenosine analogs in D1-Bx cells and an increase in cytosine analogs in D1-Mia cells. A decrease in myo-inositol was another key metabolic change in D1-Mia that was unaffected in D1-Bx.

Significantly altered spectral features were also identified in the exometabolome by comparing 1D ^{1}H NMR spectra of spent media from WT and D1 cells. Statistically significant ($p < 0.01$) bin changes are marked on the mean NMR spectra shown in Figure S2C and Figure S2D for WT-Bx and WT-Mia spent media, respectively. Intracellular metabolic shifts in branched-chain amino acids, glutamine, glutamate, glucose, and energy metabolites were also observed in the spent media (Figure S2C,D) with increased branched-chain amino acids, increased lactate excretion, increased glucose uptake, and decreased energy metabolites.

DNAJA1 overexpression significantly alters glycolytic intermediates, nucleotides, redox balance currency, and branched-chain amino acids in PDAC cells. Untargeted metabolomics analyses confirmed DNAJA1 overexpression-impaired metabolic balance in two distinct pancreatic cancer cell lines, BxPC-3 and MIA PaCa-2. The global metabolic changes resulting from DNAJA1 overexpression revealed an additional layer of functionalities tied to the metabolic reprogramming in pancreatic cancer cells.[12]

DNAJA1 Alters the Rate of Aerobic Glycolysis and Diversifies Glucose Utilization

A crucial metabolic process in cancer cells is an altered glucose metabolism that leads to an increase in lactate and alanine output.[44] Consistent with this paradigm was our observation of a differential glucose metabolism in pancreatic cancer cells due to DNAJA1 (Figure 3A). 1D ^{1}H NMR combined with stable $^{13}C_6$-glucose tracer experiments was used to characterize the cellular metabolome and exometabolome of BxPC-3 and MIA PaCa-2 cell lines. A significant accumulation of glycolytic intermediates occurred in D1-Bx and D1-Mia (Figure 3A).

A 1D ^{1}H NMR spectrum may be uniquely employed to delineate carbon flux through metabolic pathways by quantifying the amount of ^{13}C attached to a ^{1}H by using peaks commonly referred to as ^{13}C satellites. While this technique has seen limited application in metabolomics, ^{13}C satellites offer highly valuable insights as they allow for the observation of pathway regulation and the impacts thereof.[45] In the absence of a ^{13}C-labeled tracer, ^{13}C satellites are of uniform intensity corresponding to 1.1% of the intensity of the associated ^{1}H peak. With the addition of a ^{13}C-labeled tracer, the intensity of the ^{13}C satellite peaks will increase proportionally to the amount of ^{13}C attached to the ^{1}H that has been metabolically derived from the ^{13}C-labeled tracer. Here, $^{13}C_6$-glucose is the ^{13}C-labeled tracer and can be used to monitor carbon flux by using ^{13}C satellites in 1D ^{1}H NMR spectra. A map of carbon flux (Figure 3B) through aerobic glycolysis was created by comparing ^{13}C satellite peak intensities between WT and D1 cell lines. Spectra demonstrating ^{13}C-labeled or ^{12}C-labeled lactate and alanine are shown in the bottom panel of Figure 3B.

The consumption of $^{13}C_6$-glucose from the media during cell growth led to complete ^{13}C labeling of the end products of aerobic glycolysis (i.e., alanine and lactate, Figure 3A). There was no differential labeling of individual carbons in either alanine or lactate. The resulting carbon flux analysis using the ^{13}C satellite peak intensities is summarized as a set of pie charts

https://doi.org/10.1021/acs.jproteome.1c00233
J. Proteome Res. 2021, 20, 3925−3939

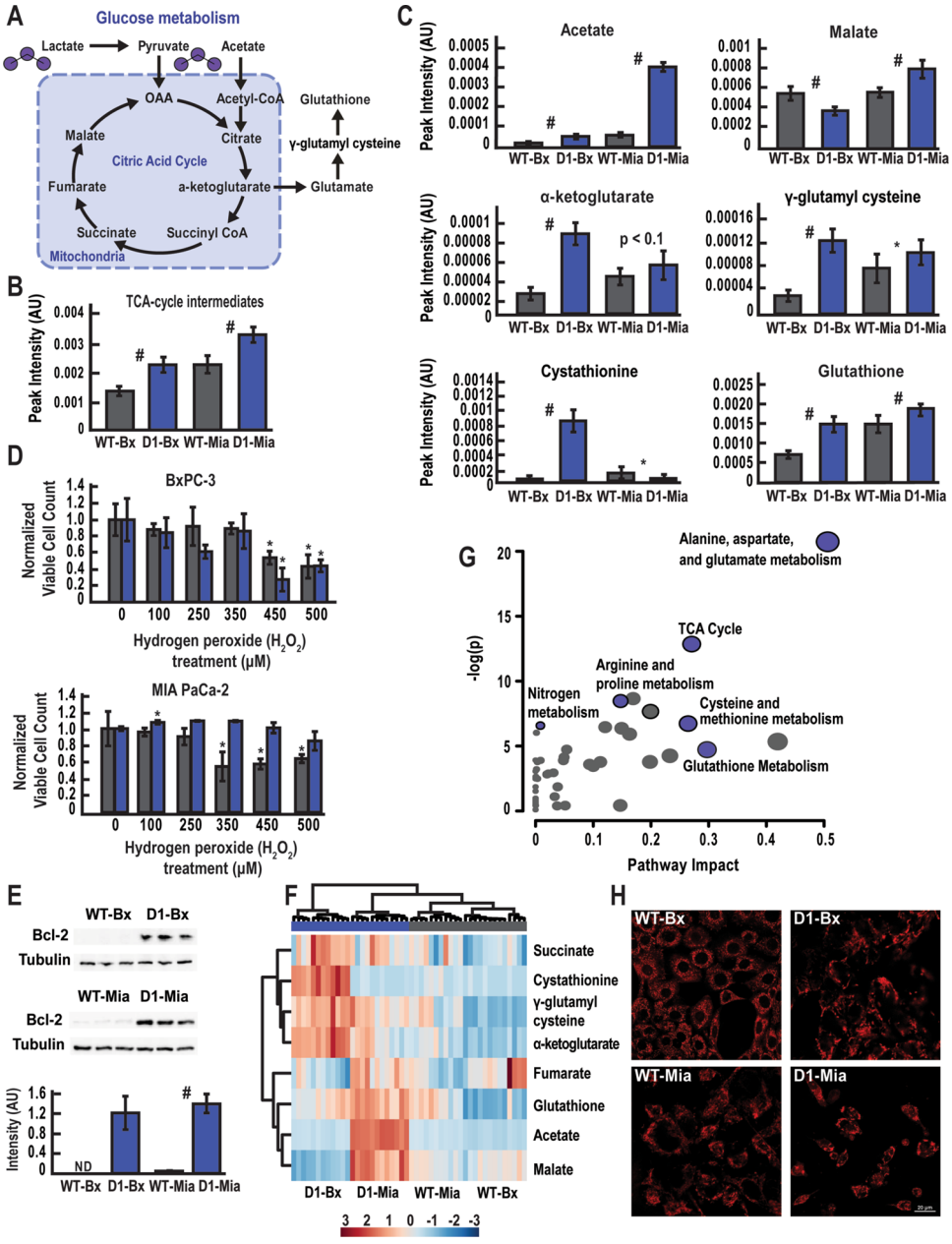

Figure 4. Disrupted redox balance fueled by an increase in TCA cycle activity in D1 overexpression. (A) Schematic of the TCA cycle illustrating the incorporation of ^{13}C carbons from glycolysis (i.e., from $^{13}C_6$-glucose) into TCA intermediates and the flow of metabolites into and out of the mitochondria. (B) Bar graph plotting the sum of NMR peak intensities for all $^{13}C_6$-glucose-derived TCA cycle intermediates obtained from 2D $^{1}H-^{13}C$ HSQC spectra. WT bars are colored gray, and D1 bars are colored blue. A statistically significant increase in TCA cycle intermediates resulted from DNAJA1 overexpression. (C) Bar charts highlighting the significant metabolic shift in TCA cycle metabolites derived from $^{13}C_6$-glucose as a result of DNAJA1 overexpression. Data are plotted as the average peak intensity from 2D $^{1}H-^{13}C$ HSQC spectra with standard deviations represented as brackets (n = 12). WT bars are colored gray, and D1 bars are colored blue. (D) Bar graph of XTT survivability assay plotted over a range (0 to 500 μM) of hydrogen peroxide treatments. Data are plotted as an average of triplicate measurements (n = 3) with standard deviations represented as brackets. WT bars are colored gray, and D1 bars are colored blue. (E) Western blot (top) analysis and bar graph quantification (bottom) of Bcl-2 induction due to DNAJA1 overexpression. Data are plotted as an average of triplicate measurements (n = 3) with standard deviations represented as brackets. ND: no data. (F) Heat map and hierarchical clustering of TCA cycle intermediates. The heat map plots normalized peak intensities from 2D $^{1}H-^{13}C$ HSQC spectra. Each row displays the relative metabolite abundance across the four groups, where red identifies a relative metabolite accumulation and blue indicates metabolite depletion. (G) Pathway impact plot based on metabolite occurrence from the analysis of the 2D $^{1}H-^{13}C$ HSQC spectra. Pathways were selected to highlight the intracellular metabolic variations linked to glucose metabolism. See Figure S4 for the complete list of pathways enriched by DNAJA1 overexpression. The pathway impact plot was generated using MetaboAnalyst 4.0 (https://www.metaboanalyst.ca/). (H) Live-cell confocal microscopy images of the mitochondria from WT and D1 cells using MitoTracker Red. Univariate pairwise comparisons used Student's t test followed by a Benjamini–Hochberg multiple-hypothesis correction. The corrected p-values are indicated as $^{*}p < 0.05$, $^{**}p < 0.01$, $^{***}p < 0.001$, and $^{\#}p < 0.0001$.

in the top panels of Figure 3B. Each pie chart arc quantifies the amount of ^{13}C-labeled or ^{12}C-labeled metabolite measured in WT, D1, and as a composite for each cell line. The amount of ^{13}C-labeled lactate derived from $^{13}C_6$-glucose remained

https://doi.org/10.1021/acs.jproteome.1c00233
J. Proteome Res. 2021, 20, 3925−3939

unchanged in D1-Bx but increased in D1-Mia. ^{13}C-Labeled alanine was increased in both D1 cell lines. Increased $^{13}C_6$-glucose-derived products indicate that DNAJA1 induced an increase in glucose consumption, which led to an accumulation of intracellular lactate and alanine.

Although the two D1 cell lines produced a comparable amount of ^{13}C lactate, there was a notable difference in the production of ^{13}C alanine where D1-Bx produced a greater amount of ^{13}C alanine than D1-Mia. This suggests that DNAJA1 skews BxPC-3 toward alanine production, while MIA PaCa-2 is directed to lactate. Investigations into PDAC cellular communication has shown that stellate cells provide alanine to pancreatic cancer cells in order to promote tumor progression and metastasis.[20] This increase in alanine in D1-Bx supports increased cellular invasion and survival, which is discussed further in the following sections.

The change in glucose utilization and in the production of alanine and lactate implies that DNAJA1 may regulate the relative activity of glycolytic enzymes including lactate dehydrogenase (LDH) and alanine aminotransferase (ALT). Alterations in the relative LDH/ALT activity would impact the cellular concentrations of pyruvate and consequently the amount of alanine and lactate produced. A resulting change in pyruvate consumption would also impact NAD^+/NADH balance, which is evident by a decrease in cellular NADH (Figure 2) and an increase in excreted lactate (Figure S3). A proper NAD^+/NADH balance is crucial for redox signaling, which may be influenced by DNAJA1. This NAD^+/NADH balance is driven by pyruvate metabolism through the malate−aspartate shuttle, by lactate production, and by nonessential amino acid synthesis. A resulting increase in NAD^+/NADH may contribute to a reduction in redox stress.[46]

A systematic analysis of 2D ^{1}H−^{13}C HSQC spectra further characterized metabolic differences between WT and D1 cell lines. Representative overlays of expanded views of the 2D ^{1}H−^{13}C HSQC spectra are shown in Figure 3C for a select set of metabolites. Their associated bar graphs (Figure 3C) and heat map (Figure 3D) plot the average relative peak intensities from the 2D ^{1}H−^{13}C HSQC spectra. A detailed list of all observed and altered metabolites, along with the statistical significance, is tabulated in the Supporting Information (Table S1). Heat maps summarizing all changes in cellular (Figure S4A) and excreted metabolites (Figure S5A) detected in the 2D ^{1}H−^{13}C HSQC spectra are also provided in the Supporting Information.

An increase in glycolytic intermediates (Figure 3A) in D1 cells shows that lactate and pyruvate were increased in the intracellular metabolome (Figure 3C,D) and exometabolome (Figure S5A), while the amount of glucose was decreased. These observations support an increased aerobic glycolysis in response to DNAJA1. DNAJA1-induced metabolic changes are further evidenced by pathway impact maps (Figure 3E) and concentration-dependent enrichment of disease pathways (Figure 3F) generated from a list of identified, dysregulated metabolites. The two distinct network analyses yielded comparable results and identified glycolysis and other key metabolic processes previously implicated (e.g., alanine metabolism, pyruvate metabolism, nicotinate and nicotinamide metabolism, and purine metabolism). Network analyses also highlighted other metabolic processes logically coupled to glycolysis, such as glutamate metabolism, starch and sucrose metabolism, fructose and mannose metabolism, and the glucose−alanine cycle. These ancillary pathways may serve to replenish or regulate the supply of glucose or supplement glycolysis. The complete, detailed network analyses of dysregulated intracellular metabolome (Figure S4B,C) and exometabolome (Figure S5B,C) are provided in the Supporting Information.

Loss of Mitochondrial Dispersion and a Disrupted Redox Balance Are Fueled by an Increased TCA Cycle Activity Induced by DNAJA1 Overexpression

The analysis of 2D ^{1}H−^{13}C HSQC spectra also identified a significant increase in glucose-derived TCA intermediates in D1-Bx and D1-Mia (Figure 4A), which suggested an increase in mitochondrial oxidative phosphorylation (OXPHOS). Despite a preference for aerobic glycolysis, TCA paired with OXPHOS is still an important source of energy production and redox balance in PDAC cells.[47,48] An increase in metabolites from TCA and OXPHOS that maintain redox balance were observed in D1 cells (Figure 4B), showing increases in acetate, α-ketoglutarate, cystathionine, γ-glutamyl cysteine, malate, γ-glutamyl cysteine, and glutathione (Figure 4C).

The hierarchical clustering of a heat map generated from TCA intermediates highlighted the relative metabolome differences between WT and D1 cells (Figure 4F). WT cells exhibited the greatest commonalities in the dendrogram, while D1-Mia and D1-Bx cells occupied independent branches. TCA intermediates were the most perturbed metabolites in D1-Bx as its branch exhibited the greatest distance from the other three cell lines. D1-Mia also demonstrated metabolome perturbations compared to WT but to a lesser degree than D1-Bx. A pathway impact map further highlighted that the TCA cycle and associated pathway shunts were the most perturbed pathways that differentiate WT from D1 cells (Figure 4G). Other metabolic processes associated with the TCA cycle and OXPHOS were identified from the network analyses (Figure S4) of the entire set of dysregulated metabolites (Table S1). DNAJA1 was shown to induce a similar increase in TCA cycle activity for both BxPC-3 and MIA PaCa-2. Differential accumulation of malate occurred at the 10 and 24 h time points between the D1-Bx and D1-Mia cells (Figure 4C). The time-dependent difference in malate may be attributed to differences in OXPHOS and malate−aspartate shuttle activity between D1-Bx and D1-Mia.

A temporally dependent accumulation of glutathione and the glutathione precursor, γ-glutamyl cysteine, occurred in D1 cells. Glutathione levels increased from two-fold to four-fold relative to WT during a 24 h growth period. An increase in glutathione combated the increase in redox stress from OXPHOS and was also associated with increased cellular proliferation and drug resistance. This time-dependent accumulation of redox currency suggested a higher oxidative stress environment upon DNAJA1 overexpression and, consequently, an increase in redox agents to relieve this stress. The elevated glutathione levels also indicated that D1 cells have an increased redox capacity, which was further supported by the survivability assay data (Figure 4D). WT-MIA cells were more susceptible to redox-induced cell death in which WT cells had decreased survivability at lower peroxide concentrations compared to D1-MIA. D1-Bx and WT-Bx showed comparable survivability under H_2O_2 stress with D1-Bx demonstrating greater recovery at higher concentrations. This supports the proposition that D1 cells have a greater redox stress capacity and greater survivability.

https://doi.org/10.1021/acs.jproteome.1c00233
J. Proteome Res. 2021, 20, 3925−3939

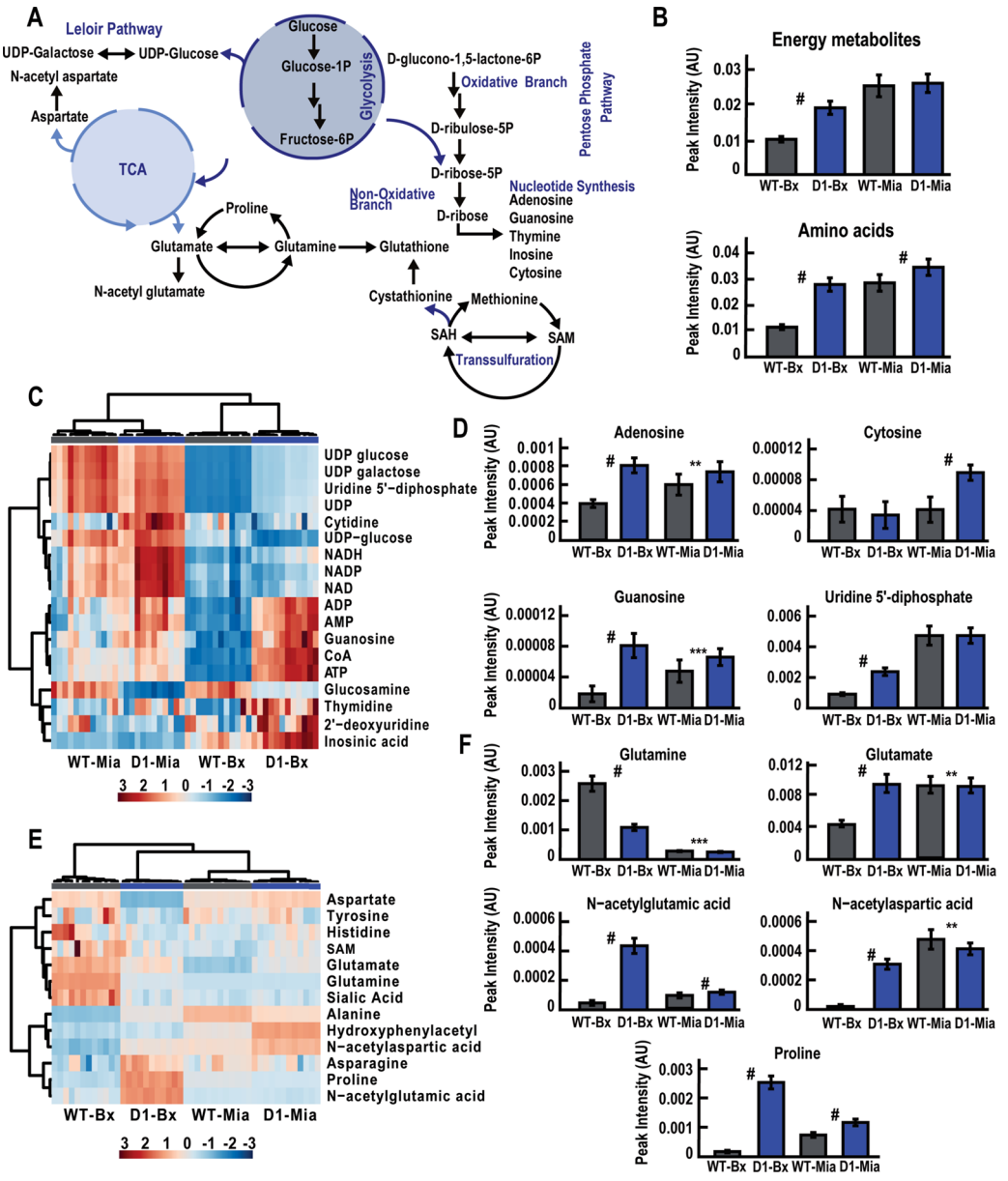

Figure 5. Aberrant amino acid metabolism coupled to a loss of cell structure results in an increase in cell invasiveness from DNAJA1 overexpression. (A) Illustration of the metabolic network that encompasses the biosynthesis of nucleotides and amino acid (e.g., glycolysis, Leloir pathway, pentose phosphate pathway, TCA cycle, etc.). The metabolic network identifies possible pathways of ^{13}C carbon incorporation into amino acids and nucleotides as derived from $^{13}C_6$-glucose. (B) Bar graphs plotting the sum of NMR peak intensities for all $^{13}C_6$-glucose-derived nucleotides (i.e., energy metabolites) and amino acid intermediates obtained from 2D $^{1}H-^{13}C$ HSQC spectra. WT bars are colored gray, and D1 bars are colored blue. A statistically significant increase in nucleotides and amino acids was observed for D1-Bx, while only a modest increase in amino acids occurred for D1-Mia. Heat map and hierarchical clustering analysis of (C) nucleotides and (E) amino acid intermediates. The heat map plots normalized peak intensities from 2D $^{1}H-^{13}C$ HSQC spectra (n = 12, n = 11 for WT-Bx). Each row displays the relative metabolite abundance across the four groups, where red identifies a relative metabolite accumulation and blue indicates metabolite depletion. Bar charts highlighting the significant metabolic shift in (D) nucleotides and (F) amino acids derived from $^{13}C_6$-glucose. Data are plotted as the average peak intensity from 2D $^{1}H-^{13}C$ HSQC spectra with standard deviations represented as brackets (n = 12).

An increase in cystathionine (Figure 4C), while only evident in D1-Bx, has been shown to inhibit ROS-induced apoptosis in breast cancer, leukocytes, and macrophages.[49−51] In breast cancer, high levels of cystathionine were found to rescue mitochondrial integrity, promote respiration, and inhibit apoptosis.[49] Increased cystathionine has also been shown to alter mitochondrial morphology in ovarian cancer.[52] These reported impacts of cystathionine and its significant increase in D1-Bx may therefore contribute to a fused mitochondrial network and additionally supported the higher mitochondrial stress in D1-Bx compared to D1-Mia.

DNAJA1 overexpression also resulted in a significant increase in the expression of Bcl-2 (Figure 4E). Increased expression of Bcl-2 has been reported to promote mitochondrial fusion and an antiapoptotic state in ovarian, breast, and prostate cancers.[53] Similarly, Bcl-2 overexpression in MIA PaCa-2 has been previously reported to lead to an increase in the metastatic phenotype and apoptotic resistance and has resulted in overall larger tumors.[54] The observed increases in

https://doi.org/10.1021/acs.jproteome.1c00233
J. Proteome Res. 2021, 20, 3925−3939

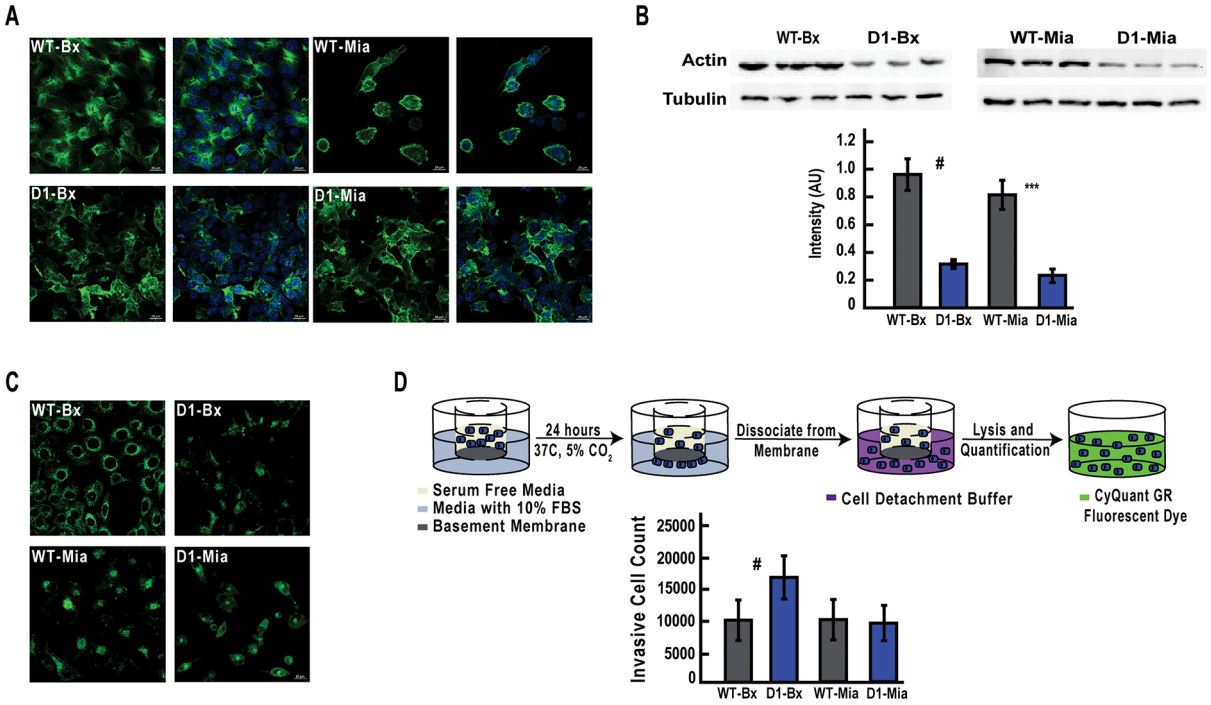

Figure 6. (A) Fixed-cell confocal microscopy images of actin filament variations (green) and nuclei (blue) between WT and D1 cells. (B) Western blot (top) analysis and bar graph quantification (bottom) of actin expression in WT and D1 cells. Data are plotted as an average of triplicate measurements (n = 3) with standard deviations represented as brackets. Univariate pairwise comparisons used a Student's t test followed by a Benjamini−Hochberg multiple-hypothesis correction. The corrected p-values are indicated as $^{*}p < 0.05$, $^{**}p < 0.01$, $^{***}p < 0.001$, and $^{\#}p < 0.0001$. (C) Live-cell confocal microscopy images of lysosomes from WT and D1 cells using LysoTracker Deep Red. (D) (top) Schematic of the invasion assay methodology. (bottom) Bar graph quantitation of cell invasiveness. Data are plotted as the number of cells present in the basement membrane with standard deviations represented as brackets (n = 3).

cystathionine, glutathione, and Bcl-2, which are all prosurvival factors, suggested that DNAJA1 may promote an antiapoptotic state in PDAC cells. The significant increase in cystathionine in D1-Bx along with a qualitative analysis of mitochondrial integrity by confocal microscopy has suggested that the antiapoptotic effect of DNAJA1 may be more aberrant in BxPC-3 than in MIA PaCa-2.

Confocal microscopy imaging of WT and D1 cells demonstrated altered mitochondrial networks in which D1-Bx appeared to be more fused than D1-Mia (Figure 4H). Mitochondrial fusion is consistent with an increase in Bcl-2 expression, cystathionine levels, and redox stress. The relative extent of mitochondrial fusion is also consistent with differential cystathionine levels between D1-Bx and D1-Mia. Mitochondrial fusion has disputed implications in cellular survival roles but in conjunction with other prosurvival factors appears to function as a promoter of cell survival in D1-Bx and D1-Mia.[53,55]

Aberrant Amino Acid Metabolism and the Subsequent Loss of Cell Structure from DNAJA1 Overexpression

The fate of $^{13}C_6$-glucose metabolism in D1 cells resulted in variable biosynthesis of prometastatic metabolites, nucleotides, and cytoskeletal components that together provided a pathway to enhanced survivability (Figure 5A). A prosurvival metabolic shift was further evidenced by an overall increase in energy metabolites and amino acids (Figure 5B). A heat map (Figure 5C) summarizing the overall changes in metabolites related to energy production illustrates that the inherent difference between the BxPC-3 and MIA PaCa-2 cell lines dominated the dendrogram structure. D1 cells were clustered with their WT counterparts on separate branches, yet both D1 lines showed significant increases in adenosine and guanosine (Figure 5D). The increase in adenosine again supports an increase in OXPHOS, which has been previously evidenced in PDAC.[56] Conversely, cytosine was significantly increased in D1-Mia, while uridine 5′-diphosphate was increased in D1-Bx, suggesting cell line-specific growth needs. A global increase in amino acid synthesis in both D1 cells (Figure 5B) highlighted a prometastasis metabolic shift, which also included an observed increase in N-acetylation, transsulfuration, and redox capacity and an alteration in cytoskeletal protein synthesis. A heat map (Figure 5E) summarizing overall changes in the metabolites related to amino acid synthesis demonstrates that the cell type again dominated the dendrogram structure. N-terminal acetylation, which relies on the availability of *N*-acetyl aspartate and *N*-acetyl glutamate, has been associated with an increase in cancer metastasis. Notably, D1 cells showed a significant variation in *N*-acetyl aspartate and *N*-acetyl glutamate (Figure 5F).[57,58] *N*-acetyl glutamate and *N*-acetyl aspartate also serve as glutamine reservoirs, which is consistent with the significant decrease in glutamine in D1 cells (Figure 5F). *N*-acetyl glutamate and *N*-acetyl aspartate are also stored as *N*-acetyl-aspartyl-glutamate (NAAG), which is correlated with an increase in cancer aggressiveness.[59,60] In prostate and colon cancer, NAAG peptidase overexpression has been shown to increase cellular migration and invasion.[59,60]

Increased redox capacity (Figure 2) was again supported by a DNAJA1-induced change in glutamine and glutamate (Figure 5F).[50] In D1 cells, glutamine was significantly decreased, but its glutamate product was only significantly increased in D1-Bx. Glutamate is required for glutathione synthesis, which is an

https://doi.org/10.1021/acs.jproteome.1c00233
J. Proteome Res. 2021, 20, 3925−3939

essential component for maintaining redox balance and is consistent with the significant increase in glutathione for D1-Bx and D1-Mia (Figure 4C). Glutamate can also be shuttled into the TCA cycle via α-ketoglutarate conversion to support an increase in OXPHOS.

A significant increase was seen for proline in both D1 cells with a 12-fold increase in D1-Bx and a 1.5-fold increase in D1-Mia. The interconversion of glutamate and proline is controlled by the c-Myc oncogene, which is a master regulator of cancer metabolism.[61] The role of proline in oncogenesis remains unclear, but the expression of c-Myc in cancer cells leads to an excess of proline for growth requirements.[62] Proline may serve as an oxidation mediator of NADPH to restore $NADP^+$, which is required for the pentose phosphate pathway (PPP). The nonoxidative PPP is responsible for nucleotide synthesis in oncogenic KRAS cancers such as MIA PaCa-2.[62] The observed increase in $NADP^+$ and nucleosides (A, G, and C) in D1-Mia (Figure 5C,D) suggests that DNAJA1 activity increased the impact of KRAS mutations and consequently promoted cell replication. D1-Bx did not exhibit a significant change in $NADP^+$ but demonstrated a dramatic 12-fold increase in proline. Proline is a precursor in actin synthesis, and the accumulation of proline in D1 cells suggests decreased synthesis of actin.[62] Cytoskeletal changes resulting from depletion in actin and the formation of locally polymerized actin are a hallmark of increased cancer invasion and metastasis.[63] Supportive of an invasive or metastatic phenotype for D1 cells was the observation that D1 cells were less adherent and exhibited increased proline accumulation compared to WT. Phalloidin staining of fixed cells imaged by confocal microscopy further confirmed the presence of stunted actin filaments in D1-overexpressing cells (Figure 6A). While this difference is modest in D1-Mia cells, both D1 cells showed a qualitative lack of mature actin filaments. Western blot analysis (Figure 6B) quantification demonstrated a significant decrease in actin for both D1-Bx and D1-Mia.

Lysosomes play important regulatory roles in cytoskeleton composition, cancer invasion, and cancer metastasis. Weaker lysosomal membranes promote these events and are generally associated with cancer.[64] Confocal microscopy images of lysosomes from WT and D1 cells showed a decrease in the lysosomal dye intensity in D1 cells, suggesting weaker lysosomal membranes in response to increased DNAJA1 (Figure 6C). An apparent loss in nuclear localization in D1 cells also supports an increase in cell aggressiveness.[64,65] This lysosomal dispersion and weakened membranes suggested that DNAJA1 may be impacting the regulatory role of HSP70 in autophagy, which is a required process in the metabolic reprogramming of PDAC. Disassembled actin filaments, lysosomal variation, an increase in redox capacity, and an accumulation of proline and other metastatic metabolites suggested an invasive phenotype due to DNAJA1. An invasion assay using a basement membrane (Figure 6D) showed that D1-Bx cells were significantly more invasive than WT-Bx, but no difference was observed for D1-Mia. The lack of an increase in D1-Mia invasiveness is consistent with the qualitative microscopic observations and the less drastic variation in invasive and metastatic metabolites that exhibited pronounced changes in D1-Bx cells.

CONCLUSIONS

The downregulation of DNAJA1 expression in PDAC identified this protein as a potential therapeutic target. While DNAJA1 has demonstrated increased tumorigenicity upon decreased expression in C6 glioblastoma, DNAJA1 overexpression did not inhibit PDAC growth.[18] Instead, DNAJA1 in PDAC appears to behave as reported in colorectal cancer, which demonstrated an increase in cellular proliferation, invasion, and metastasis.[66] Conflicting outcomes of DNAJA1 expression suggest that its cellular roles may be dependent on other tumor-suppressing or proto-oncogenic partners unique to each cancer type. Here, we reported a detailed metabolomics study of two genotypically distinct cancer cell lines overexpressing DNAJA1 that when combined with confocal microscopy, flow cytometry, and cell-based assays suggests an oncogenic role for DNAJA1 in PDAC.[14]

Overexpression of DNAJA1 promoted the Warburg effect, which resulted in increased glucose consumption for the production of metabolites that promote cellular proliferation. Our SIRM approach identified a decrease in $^{13}C_6$-glucose and a subsequent increase in the production of lactate, pyruvate, alanine, fructose-6-phosphate, and PEP. We also observed an increase in energy metabolites (e.g., NAD and NADP) to maintain glycolysis. DNAJA1 also impacted TCA cycle intermediates, which promoted mitochondrial network fusion, antiapoptosis, and increased redox tolerance. Overall, these metabolic changes support DNAJA1 serving a proto-oncogenic role in PDAC and are inconsistent with a simple metabolic signature of protein overexpression.[42,43,67] A future detailed flux analysis may prove valuable for the further characterization of these metabolic changes. D1 cells presented apparent weaker lysosomal membranes, decreased actin filament formation, and increased invasion relative to WT. All these alterations led to the identification of morphological changes in PDAC cells overexpressing DNAJA1 and suggest that DNAJA1 has numerous regulatory roles that influence cellular growth and proliferation. Unexpectedly, the overexpression of DNAJA1 was not detrimental to the BxPC-3 and MIA PaCa-2 cells and actually appeared to be beneficial. Thus, the downregulation of DNAJA1 in PDAC is perplexing, and our results do not provide any clear insights into a mechanism that may explain this decrease in expression levels. As noted above, these conflicting results may derive from a complex functional synergy between DNAJA1 and other tumor-suppressing or proto-oncogenic partners that may also be differentially regulated in cancer cells. A planned investigation to identify DNAJA1 binding partners may provide important insights into the mechanisms by which DNAJA1 induces these cellular changes.

While the overall influence of DNAJA1 on BxPC-3 and MIA PaCa-2 cells was comparable, the magnitude of the effect varied with some differences specific to D1-Bx or D1-Mia. The global metabolic profiles were still dominated by genotype differences between BxPC-3 and MIA PaCa-2 PDAC cell lines. The most notable difference caused by DNAJA1 overexpression was the relative change in cell invasiveness, where D1-Bx cells were significantly more invasive and D1-Mia invasiveness was unchanged. The dissimilar response to DNAJA1 is likely attributed to the inherent genotype differences between the BxPC-3 and MIA PaCa-2 PDAC cell lines. BxPC-3 exhibits a homozygous deletion of SMAD4 and a mutant TP53, while MIA PaCa-2 exhibits a mutant KRAS and a mutant TP53.[19] The depletion of SMAD4 in PDAC has been previously shown to increase invasiveness and metastasis in PDAC, where a mutant KRAS is the initiating event in PDAC and is required for tumorigenesis.[68,69] Thus, KRAS and

https://doi.org/10.1021/acs.jproteome.1c00233
J. Proteome Res. 2021, 20, 3925−3939

SMAD4 mutations contribute to metabolic differences and alterations in invasiveness, where DNAJA1 overexpression seemed to enhance these differences.

A range of cellular and physiological functions have been attributed to the HSP40 family of proteins with increasing evidence that their chaperone activity contributes to pathological processes. HSP40 client proteins are predominantly tumor-suppressing or proto-oncogenic.[13] In this regard, HSP40 chaperone clients may offer valuable drug targets. Here, we have demonstrated the numerous metabolic impacts that DNAJA1 exerts in PDAC and suggest multiple roles of DNAJA1 in oncogenic processes.

■ ASSOCIATED CONTENT

Supporting Information

The Supporting Information is available free of charge at https://pubs.acs.org/doi/10.1021/acs.jproteome.1c00233.

Metabolite identification and related statistics for cell lysates (Table S1); metabolite identification and related statistics for cell media (Table S2); metabolite average concentrations and standard deviations from cell lysates (Table S3); metabolite average concentrations and standard deviations from cell media (Table S4); unique exometabolome of pancreatic cancer cells following DNAJA1 overexpression (Figure S1); global metabolic changes observed extracellularly following DNAJA1 overexpression (Figure S2); OPLS models generated from 1D ^{1}H NMR cell lysates and media (Figure S3); summary of all ^{13}C glucose-derived intracellular metabolic changes in DNAJA1 overexpression (Figure S4); summary of all ^{13}C glucose-derived extracellular metabolic changes in DNAJA1 overexpression (Figure S5); image of the entire Western blot membrane showing DNAJA1 in MIA PaCa-2 that was edited to form Figure 1B (Figure S6); image of the entire Western blot membrane showing tubulin in MIA PaCa-2 that was edited to form Figure 1B (Figure S7); image of the entire Western blot membrane showing DNAJA1 in BxPC-3 that was edited to form Figure 1B (Figure S8); image of the entire Western blot membrane showing tubulin in BxPC-3 that was edited to form Figure 1B (Figure S9) (PDF)

■ AUTHOR INFORMATION

Corresponding Author

Robert Powers − *Department of Chemistry, Nebraska Center for Integrated Biomolecular Communication, and Redox Biology Center, University of Nebraska-Lincoln, Lincoln, Nebraska 68588-0304, United States;* orcid.org/0000-0001-9948-6837; Phone: (402) 472-3039; Email: rpowers3@unl.edu; Fax: (402) 472-9402

Authors

Heidi E. Roth − *Department of Chemistry, University of Nebraska-Lincoln, Lincoln, Nebraska 68588-0304, United States*

Fatema Bhinderwala − *Department of Chemistry and Nebraska Center for Integrated Biomolecular Communication, University of Nebraska-Lincoln, Lincoln, Nebraska 68588-0304, United States;* Present Address: Department of Structural Biology, University of Pittsburgh School of Medicine, Pittsburgh, Pennsylvania 15213, United States (F.B.)

Rodrigo Franco − *School of Veterinary Medicine and Biomedical Sciences, University of Nebraska-Lincoln, Lincoln, Nebraska 68583-0905, United States; Redox Biology Center, University of Nebraska-Lincoln, Lincoln, Nebraska 68588-0304, United States*

You Zhou − *Nebraska Center for Integrated Biomolecular Communication, University of Nebraska-Lincoln, Lincoln, Nebraska 68588-0304, United States; Morrison Microscopy Core Research Facility, University of Nebraska-Lincoln, Lincoln, Nebraska 68588-0664, United States*

Complete contact information is available at: https://pubs.acs.org/10.1021/acs.jproteome.1c00233

Author Contributions

$^{\nabla}$H.R. and F.B. contributed equally to the work.

Author Contributions

H.R. and F.B. performed the experiments and analyzed the data. H.R., F.B., and R.P. conceived the project. Y.Z. assisted in microscopy work, and R.F. assisted with Western blot analyses. H.R., F.B., and R.P. wrote and edited the manuscript.

Notes

The authors declare no competing financial interest.

■ ACKNOWLEDGMENTS

We would like to thank Dr. Pankaj Singh at the University of Nebraska Medical Center for his gift of the DNAJA1 Phoenix cells used in this study. We would also like to thank Dr. Martha Morton, Director of the Molecular Analysis and Characterization Facility within the Department of Chemistry at the University of Nebraska-Lincoln, for her assistance in acquiring NMR data. We want to thank the staff at the Morrison Microscopy Core Facility at the University of Nebraska-Lincoln for their assistance in completing the confocal microscopy imaging and the Flow Cytometry Core Facility for flow cytometry analyses. This work was supported in part by funding from the Nebraska Center for Integrated Biomolecular Communication (P20 GM113126, NIGMS). The research was performed in facilities renovated with support from the National Institutes of Health (RR015468-01).

■ REFERENCES

(1) American Cancer Society, Cancer Statistics Center. http://cancerstatisticscenter.cancer.org, Accessed May 2020.

(2) Hosein, A. N.; Beg, M. S. Pancreatic Cancer Metabolism: Molecular Mechanisms and Clinical Applications. *Curr. Oncol. Rep.* **2018**, *20*, 56.

(3) Long, J.; Zhang, Y.; Yu, X.; Yang, J.; LeBrun, D. G.; Chen, C.; Yao, Q.; Li, M. Overcoming drug resistance in pancreatic cancer. *Expert Opin. Ther. Targets* **2011**, *15*, 817−828.

(4) Kleeff, J.; Korc, M.; Apte, M.; La Vecchia, C.; Johnson, C. D.; Biankin, A. V.; Neale, R. E.; Tempero, M.; Tuveson, D. A.; Hruban, R. H.; Neoptolemos, J. P. Pancreatic cancer. *Nat. Rev. Dis. Primers* **2016**, *2*, 16022.

(5) Gebregiworgis, T.; Bhinderwala, F.; Purohit, V.; Chaika, N. V.; Singh, P. K.; Powers, R. Insights into gemcitabine resistance and the potential for therapeutic monitoring. *Metabolomics* **2018**, *14*, 156.

(6) Amrutkar, M.; Gladhaug, I. Pancreatic Cancer Chemoresistance to Gemcitabine. *Cancers* **2017**, *9*, 157.

(7) Nakano, Y.; Tanno, S.; Koizumi, K.; Nishikawa, T.; Nakamura, K.; Minoguchi, M.; Izawa, T.; Mizukami, Y.; Okumura, T.; Kohgo, Y.

Gemcitabine chemoresistance and molecular markers associated with gemcitabine transport and metabolism in human pancreatic cancer cells. *Br. J. Cancer* **2007**, *96*, 457−463.
(8) Qin, C.; Yang, G.; Yang, J.; Ren, B.; Wang, H.; Chen, G.; Zhao, F.; You, L.; Wang, W.; Zhao, Y. Metabolism of pancreatic cancer: paving the way to better anticancer strategies. *Mol. Cancer* **2020**, *19*, 50.
(9) Beger, R. A review of applications of metabolomics in cancer. *Metabolites* **2013**, *3*, 552−574.
(10) Bruntz, R. C.; Lane, A. N.; Higashi, R. M.; Fan, T. W. M. Exploring cancer metabolism using stable isotope-resolved metabolomics (SIRM). *J. Biol. Chem.* **2017**, *292*, 11601−11609.
(11) Bhinderwala, F.; Powers, R. NMR Metabolomics Protocols for Drug Discovery. *Methods Mol. Biol.* **2019**, *2037*, 265−311.
(12) Alderson, T. R.; Kim, J. H.; Markley, J. L. Dynamical Structures of Hsp70 and Hsp70-Hsp40 Complexes. *Structure* **2016**, *24*, 1014−1030.
(13) Sterrenberg, J. N.; Blatch, G. L.; Edkins, A. L. Human DNAJ in cancer and stem cells. *Cancer Lett.* **2011**, *312*, 129−142.
(14) Crnogorac-Jurcevic, T.; Gangeswaran, R.; Bhakta, V.; Capurso, G.; Lattimore, S.; Akada, M.; Sunamura, M.; Prime, W.; Campbell, F.; Brentnall, T. A.; Costello, E.; Neoptolemos, J.; Lemoine, N. R. Proteomic analysis of chronic pancreatitis and pancreatic adenocarcinoma. *Gastroenterology* **2005**, *129*, 1454−1463.
(15) Niu, G.; Zhang, H.; Liu, D.; Chen, L.; Belani, C.; Wang, H. G.; Cheng, H. Tid1, the Mammalian Homologue of Drosophila Tumor Suppressor Tid56, Mediates Macroautophagy by Interacting with Beclin1-containing Autophagy Protein Complex. *J. Biol. Chem.* **2015**, *290*, 18102−18110.
(16) Ahn, B. Y.; Trinh, D. L. N.; Zajchowski, L. D.; Lee, B.; Elwi, A. N.; Kim, S.-W. Tid1 is a new regulator of p53 mitochondrial translocation and apoptosis in cancer. *Oncogene* **2010**, *29*, 1155−1166.
(17) Stark, J. L.; Mehla, K.; Chaika, N.; Acton, T. B.; Xiao, R.; Singh, P. K.; Montelione, G. T.; Powers, R. Structure and function of human DnaJ homologue subfamily a member 1 (DNAJA1) and its relationship to pancreatic cancer. *Biochemistry* **2014**, *53*, 1360−1372.
(18) Meshalkina, D. A.; Shevtsov, M. A.; Dobrodumov, A. V.; Komarova, E. Y.; Voronkina, I. V.; Lazarev, V. F.; Margulis, B. A.; Guzhova, I. V. Knock-down of Hdj2/DNAJA1 co-chaperone results in an unexpected burst of tumorigenicity of C6 glioblastoma cells. *Oncotarget* **2016**, *7*, 22050−22063.
(19) Deer, E. L.; Gonzalez-Hernandez, J.; Coursen, J. D.; Shea, J. E.; Ngatia, J.; Scaife, C. L.; Firpo, M. A.; Mulvihill, S. J. Phenotype and genotype of pancreatic cancer cell lines. *Pancreas* **2010**, *39*, 425−435.
(20) Vaziri-Gohar, A.; Zarei, M.; Brody, J. R.; Winter, J. M. Metabolic Dependencies in Pancreatic Cancer. *Front. Oncol.* **2018**, *8*, 617.
(21) Thompson, E. J.; Shanmugam, K.; Hattrup, C. L.; Kotlarczyk, K. L.; Gutierrez, A.; Bradley, J. M.; Mukherjee, P.; Gendler, S. J. Tyrosines in the MUC1 cytoplasmic tail modulate transcription via the extracellular signal-regulated kinase 1/2 and nuclear factor-kappaB pathways. *Mol. Cancer Res.* **2006**, *4*, 489−497.
(22) Dai, X.; Yu, X.; Gong, H.; Jiang, X.; Abenes, G.; Liu, H.; Shivakoti, S.; Britt, W. J.; Zhu, H.; Liu, F.; Zhou, Z. H. The smallest capsid protein mediates binding of the essential tegument protein pp150 to stabilize DNA-containing capsids in human cytomegalovirus. *PLoS Pathog.* **2013**, *9*, No. e1003525.
(23) Dia, X.; Zhou, Z. H. Purification of Herpesvirus Virions and Capsids. *Bio-Protoc.* **2014**, *4*, No. e1193.
(24) Son, J.; Lyssiotis, C. A.; Ying, H.; Wang, X.; Hua, S.; Ligorio, M.; Perera, R. M.; Ferrone, C. R.; Mullarky, E.; Shyh-Chang, N.; Kang, Y.; Fleming, J. B.; Bardeesy, N.; Asara, J. M.; Haigis, M. C.; DePinho, R. A.; Cantley, L. C.; Kimmelman, A. C. Glutamine supports pancreatic cancer growth through a KRAS-regulated metabolic pathway. *Nature* **2013**, *496*, 101−105.
(25) Nguyen, B. D.; Meng, X.; Donovan, K. J.; Shaka, A. J. SOGGY: Solvent-optimized double gradient spectroscopy for water suppression. A comparison with some existing techniques. *J. Magn. Reson.* **2007**, *184*, 263−274.
(26) Worley, B.; Powers, R. Deterministic multidimensional nonuniform gap sampling. *J. Magn. Reson.* **2015**, *261*, 19−26.
(27) Worley, B.; Powers, R. MVAPACK: a complete data handling package for NMR metabolomics. *ACS Chem. Biol.* **2014**, *9*, 1138−1144.
(28) Worley, B.; Powers, R. Generalized adaptive intelligent binning of multiway data. *Chemom. Intell. Lab. Syst.* **2015**, *146*, 42−46.
(29) Halouska, S.; Powers, R. Negative impact of noise on the principal component analysis of NMR data. *J. Magn. Reson.* **2006**, *178*, 88−95.
(30) Worley, B.; Halouska, S.; Powers, R. Utilities for quantifying separation in PCA/PLS-DA scores plots. *Anal. Biochem.* **2013**, *433*, 102−104.
(31) Savorani, F.; Tomasi, G.; Engelsen, S. B. icoshift: A versatile tool for the rapid alignment of 1D NMR spectra. *J. Magn. Reson.* **2010**, *202*, 190−202.
(32) Johnson, B. A.; Blevins, R. A. NMRView: A Computer Program for the Visualization and Analysis of NMR Data. *J. Biomol. NMR* **1994**, *4*, 603−614.
(33) Delaglio, F.; Grzesiek, S.; Vuister, G. W.; Zhu, G.; Pfeifer, J.; Bax, A. NMRPipe: A multidimensional spectral processing system based on UNIX pipes. *J. Biomol. NMR* **1995**, *6*, 277−293.
(34) Ying, J.; Delaglio, F.; Torchia, D. A.; Bax, A. Sparse multidimensional iterative lineshape-enhanced (SMILE) reconstruction of both non-uniformly sampled and conventional NMR data. *J. Biomol. NMR* **2017**, *68*, 101−118.
(35) Kikuchi, J.; Shinozaki, K.; Hirayama, T. Stable isotope labeling of Arabidopsis thaliana for an NMR-based metabolomics approach. *Plant Cell Physiol.* **2004**, *45*, 1099−1104.
(36) Wishart, D. S.; Jewison, T.; Guo, A. C.; Wilson, M.; Knox, C.; Liu, Y. F.; Djoumbou, Y.; Mandal, R.; Aziat, F.; Dong, E.; Bouatra, S.; Sinelnikov, I.; Arndt, D.; Xia, J. G.; Liu, P.; Yallou, F.; Bjorndahl, T.; Perez-Pineiro, R.; Eisner, R.; Allen, F.; Neveu, V.; Greiner, R.; Scalbert, A. HMDB 3.0-The Human Metabolome Database in 2013. *Nucleic Acids Res.* **2013**, *41*, D801−D807.
(37) Ulrich, E. L.; Akutsu, H.; Doreleijers, J. F.; Harano, Y.; Ioannidis, Y. E.; Lin, J.; Livny, M.; Mading, S.; Maziuk, D.; Miller, Z.; Nakatani, E.; Schulte, C. F.; Tolmie, D. E.; Kent Wenger, R.; Yao, H.; Markley, J. L. BioMagResBank. *Nucleic Acids Res.* **2007**, *36*, D402−D408.
(38) Cui, Q.; Lewis, I. A.; Hegeman, A. D.; Anderson, M. E.; Li, J.; Schulte, C. F.; Westler, W. M.; Eghbalnia, H. R.; Sussman, M. R.; Markley, J. L. Metabolite identification via the Madison Metabolomics Consortium Database. *Nat. Biotechnol.* **2008**, *26*, 162−164.
(39) Chong, J.; Wishart, D. S.; Xia, J. Using MetaboAnalyst 4.0 for Comprehensive and Integrative Metabolomics Data Analysis. *Curr. Protoc. Bioinf.* **2019**, *68*, No. e86.
(40) Rodriguez-Rocha, H.; Garcia Garcia, A.; Zavala-Flores, L.; Li, S.; Madayiputhiya, N.; Franco, R. Glutaredoxin 1 protects dopaminergic cells by increased protein glutathionylation in experimental Parkinson's disease. *Antioxid. Redox Signaling* **2012**, *17*, 1676−1693.
(41) Schneider, C. A.; Rasband, W. S.; Eliceiri, K. W. NIH Image to ImageJ: 25 years of image analysis. *Nat. Methods* **2012**, *9*, 671−675.
(42) Hergesheimer, R.; Lanznaster, D.; Bourgeais, J.; Hérault, O.; Vourc'h, P.; Andres, C. R.; Corcia, P.; Blasco, H. Conditioned Medium from Cells Overexpressing TDP-43 Alters the Metabolome of Recipient Cells. *Cell* **2020**, *9*, 2198.
(43) Yang, J.; Wang, N.; Chen, D.; Yu, J.; Pan, Q.; Wang, D.; Liu, J.; Shi, X.; Dong, X.; Cao, H.; Li, L.; Li, L. The Impact of GFP Reporter Gene Transduction and Expression on Metabolomics of Placental Mesenchymal Stem Cells Determined by UHPLC-Q/TOF-MS. *Stem Cells Int.* **2017**, *2017*, 3167985−3167985.
(44) Liberti, M. V.; Locasale, J. W. The Warburg Effect: How Does it Benefit Cancer Cells? *Trends Biochem. Sci.* **2016**, *41*, 211−218.
(45) Vinaixa, M.; Rodríguez, M. A.; Aivio, S.; Capellades, J.; Gómez, J.; Canyellas, N.; Stracker, T. H.; Yanes, O. Positional Enrichment by

https://doi.org/10.1021/acs.jproteome.1c00233
J. Proteome Res. 2021, 20, 3925−3939

Proton Analysis (PEPA): A One-Dimensional ^{1}H-NMR Approach for ^{13}C Stable Isotope Tracer Studies in Metabolomics. *Angew. Chem., Int. Ed. Engl.* **2017**, *56*, 3531−3535.
(46) Blacker, T. S.; Duchen, M. R. Investigating mitochondrial redox state using NADH and NADPH autofluorescence. *Free Radical Biol. Med.* **2016**, *100*, 53−65.
(47) Yan, L.; Raj, P.; Yao, W.; Ying, H. Glucose metabolism in pancreatic cancer. *Cancers* **2019**, *11*, 1460.
(48) Jose, C.; Bellance, N.; Rossignol, R. Choosing between glycolysis and oxidative phosphorylation: A tumor's dilemma. *Biochim. Biophys. Acta, Bioenerg.* **2011**, *1807*, 552−561.
(49) Sen, S.; Kawahara, B.; Mahata, S. K.; Tsai, R.; Yoon, A.; Hwang, L.; Hu-Moore, K.; Villanueva, C.; Vajihuddin, A.; Parameshwar, P.; You, M.; Bhaskar, D. L.; Gomez, O.; Faull, K. F.; Farias-Eisner, R.; Chaudhuri, G. Cystathionine: A novel oncometabolite in human breast cancer. *Arch. Biochem. Biophys.* **2016**, *604*, 95−102.
(50) Traverso, N.; Ricciarelli, R.; Nitti, M.; Marengo, B.; Furfaro, A. L.; Pronzato, M. A.; Marinari, U. M.; Domenicotti, C. Role of glutathione in cancer progression and chemoresistance. *Oxid. Med. Cell. Longevity* **2013**, *2013*, 972913.
(51) Wang, X.; Wang, Y.; Zhang, L.; Zhang, D.; Bai, L.; Kong, W.; Huang, Y.; Tang, C.; Du, J.; Jin, H. L-Cystathionine Protects against Homocysteine-Induced Mitochondria-Dependent Apoptosis of Vascular Endothelial Cells. *Oxid. Med. Cell. Longevity* **2019**, *2019*, 1253289.
(52) Chakraborty, P. K.; Murphy, B.; Mustafi, S. B.; Dey, A.; Xiong, X.; Rao, G.; Naz, S.; Zhang, M.; Yang, D.; Dhanasekaran, D. N.; Bhattacharya, R.; Mukherjee, P. Cystathionine β-synthase regulates mitochondrial morphogenesis in ovarian cancer. *FASEB J.* **2018**, *32*, 4145−4157.
(53) Zamponi, N.; Zamponi, E.; Cannas, S. A.; Billoni, O. V.; Helguera, P. R.; Chialvo, D. R. Mitochondrial network complexity emerges from fission/fusion dynamics. *Sci. Rep.* **2018**, *8*, 363.
(54) Bold, R. J.; Virudachalam, S.; McConkey, D. J. BCL2 Expression Correlates with Metastatic Potential in Pancreatic Cancer Cell Lines. *Cancer* **2001**, *92*, 1122−1129.
(55) Yu, M.; Nguyen, N. D.; Huang, Y.; Lin, D.; Fujimoto, T. N.; Molkentine, J. M.; Deorukhkar, A.; Kang, Y.; San Lucas, F. A.; Fernandes, C. J.; Koay, E. J.; Gupta, S.; Ying, H.; Koong, A. C.; Herman, J. M.; Fleming, J. B.; Maitra, A.; Taniguchi, C. M. Mitochondrial fusion exploits a therapeutic vulnerability of pancreatic cancer. *JCI Insight* **2019**, *4*, No. e126915.
(56) Viale, A.; Corti, D.; Draetta, G. F. Tumors and Mitochondrial Respiration: A Neglected Connection. *Cancer Res.* **2015**, *75*, 3687.
(57) Ree, R.; Varland, S.; Arnesen, T. Spotlight on protein N-terminal acetylation. *Exp. Mol. Med.* **2018**, *50*, 1−13.
(58) Zand, B.; Previs, R. A.; Zacharias, N. M.; Rupaimoole, R.; Mitamura, T.; Nagaraja, A. S.; Guindani, M.; Dalton, H. J.; Yang, L.; Baddour, J.; Achreja, A.; Hu, W.; Pecot, C. V.; Ivan, C.; Wu, S. Y.; McCullough, C. R.; Gharpure, K. M.; Shoshan, E.; Pradeep, S.; Mangala, L. S.; Rodriguez-Aguayo, C.; Wang, Y.; Nick, A. M.; Davies, M. A.; Armaiz-Pena, G.; Liu, J.; Lutgendorf, S. K.; Baggerly, K. A.; Eli, M. B.; Lopez-Berestein, G.; Nagrath, D.; Bhattacharya, P. K.; Sood, A. K. Role of Increased n-acetylaspartate Levels in Cancer. *J. Natl. Cancer Inst.* **2016**, *108*, No. djv426.
(59) Whitaker, H. C.; Shiong, L. L.; Kay, J. D.; Grönberg, H.; Warren, A. Y.; Seipel, A.; Wiklund, F.; Thomas, B.; Wiklund, P.; Miller, J. L.; Menon, S.; Ramos-Montoya, A.; Vowler, S. L.; Massie, C.; Egevad, L.; Neal, D. E. N-acetyl-L-aspartyl-L-glutamate peptidase-like 2 is overexpressed in cancer and promotes a pro-migratory and pro-metastatic phenotype. *Oncogene* **2014**, *33*, 5274−5287.
(60) Nguyen, T.; Kirsch, B. J.; Asaka, R.; Nabi, K.; Quinones, A.; Tan, J.; Antonio, M. J.; Camelo, F.; Li, T.; Nguyen, S.; Hoang, G.; Nguyen, K.; Udupa, S.; Sazeides, C.; Shen, Y. A.; Elgogary, A.; Reyes, J.; Zhao, L.; Kleensang, A.; Chaichana, K. L.; Hartung, T.; Betenbaugh, M. J.; Marie, S. K.; Jung, J. G.; Wang, T. L.; Gabrielson, E.; Le, A. Uncovering the Role of N-Acetyl-Aspartyl-Glutamate as a Glutamate Reservoir in Cancer. *Cell Rep.* **2019**, *27*, 491−501.e6.
(61) D'Aniello, C.; Patriarca, E. J.; Phang, J. M.; Minchiotti, G. Proline Metabolism in Tumor Growth and Metastatic Progression. *Front. Oncol.* **2020**, *10*, 776.
(62) Phang, J. M.; Liu, W.; Hancock, C.; Christian, K. J. The proline regulatory axis and cancer. *Front. Oncol.* **2012**, *2*, 60.
(63) Yamaguchi, H.; Condeelis, J. Regulation of the actin cytoskeleton in cancer cell migration and invasion. *Biochim. Biophys. Acta* **2007**, *1773*, 642−652.
(64) Piao, S.; Amaravadi, R. K. Targeting the lysosome in cancer. *Ann. N. Y. Acad. Sci.* **2016**, *1371*, 45−54.
(65) Hämälistö, S.; Jäättelä, M. Lysosomes in cancer-living on the edge (of the cell). *Curr. Opin. Cell Biol.* **2016**, *39*, 69−76.
(66) Yang, S.; Ren, X.; Liang, Y.; Yan, Y.; Zhou, Y.; Hu, J.; Wang, Z.; Song, F.; Wang, F.; Liao, W.; Liao, W.; Ding, Y.; Liang, L. KNK437 restricts the growth and metastasis of colorectal cancer via targeting DNAJA1/CDC45 axis. *Oncogene* **2020**, *39*, 249−261.
(67) Choi, B.-H.; Coloff, J. L. The Diverse Functions of Non-Essential Amino Acids in Cancer. *Cancers* **2019**, *11*, 675.
(68) Liu, F. SMAD4/DPC4 and Pancreatic Cancer Survival. *Clin. Cancer Res.* **2001**, *7*, 3853−3856.
(69) Waters, A. M.; Der, C. J. KRAS: The Critical Driver and Therapeutic Target for Pancreatic Cancer. *Cold Spring Harb Perspect. Med.* **2018**, *8*, a031435.

https://doi.org/10.1021/acs.jproteome.1c00233
J. Proteome Res. 2021, 20, 3925−3939